

# New fossils reveal the hand of *Paranthropus boisei*

<https://doi.org/10.1038/s41586-025-09594-8>

Received: 27 February 2025

Accepted: 5 September 2025

Published online: 15 October 2025

Open access

 Check for updates

Carrie S. Mongle<sup>1,2</sup>✉, Caley M. Orr<sup>3,4</sup>, Matthew W. Tocheri<sup>5,6,7</sup>, Thomas Cody Prang<sup>8</sup>, Frederick E. Grine<sup>1,9</sup>, Craig Feibel<sup>10,11</sup>, Biren A. Patel<sup>12</sup>, Olivia Laureijs<sup>5</sup>, Tara E. Hobbs<sup>3</sup>, Stephanie Maiolino<sup>9</sup>, James Rossie<sup>1</sup>, Winfred Mbogo<sup>13</sup>, Anton Du Plessis<sup>14,15</sup>, John Lonyericho<sup>16</sup>, William Woto Huka<sup>16</sup>, Hilary Sale<sup>16</sup>, Abdi Umuro<sup>17</sup>, Peter Yirgudo<sup>17</sup>, Ibrae Dalacha<sup>17</sup>, Martin Kirinya<sup>16</sup>, Ezekiel Linga<sup>16</sup>, Richard Loki<sup>17</sup>, Apolo Longaye<sup>16</sup>, Malmalo Longaye<sup>16</sup>, Emmanuel Lonyericho<sup>16</sup>, Iyole Loyapan<sup>16</sup>, Nyiber Nakudo<sup>17</sup>, Cyprian Nyete<sup>16</sup>, Meave G. Leakey<sup>2,17</sup> & Louise N. Leakey<sup>1,2,17,18</sup>

When Mary Leakey discovered the OH 5 cranium of *Paranthropus boisei* alongside Oldowan stone artefacts, it was declared “the oldest yet discovered maker of stone tools”<sup>1</sup>. Whether *Paranthropus* made and used tools has been debated ever since<sup>2–4</sup>, largely because there are no known hand bones that can be definitively attributed to this genus. Here we report fossil hand and foot bones unambiguously associated with craniodental material of *P. boisei*. KNM-ER 101000 demonstrates that *P. boisei* shared key manipulative and bipedal adaptations with the genus *Homo*. Moreover, the hand morphology of KNM-ER 101000 converges on that of gorillas in ways that are consistent with manual food processing and would have facilitated powerful grasping, such as that used in climbing. These fossils suggest that *P. boisei* was capable of tool making and use in some capacity while also supporting the proposed dichotomy of distinct dietary adaptations between *Paranthropus* and *Homo*. In addition to offering insights into the poorly known postcranial functional anatomy of *Paranthropus*, this discovery illuminates broader patterns of hominin hand evolution and tool use.

In recent decades, some researchers have opined that it should be assumed until proven otherwise that all Plio-Pleistocene hominin species engaged in tool behaviours to some degree<sup>3,5–7</sup>. Meanwhile, others have argued that *Paranthropus* was a toolmaker on the basis of analyses of hand bones with uncertain attribution to the southern African species *Paranthropus robustus*<sup>8–12</sup>. However, fossil hand bones confidently associated with taxonomically diagnostic craniodental remains have been conspicuously missing from these debates. Almost none of the approximately 2.5–1.0 million-year-old hominin hand fossils from eastern Africa are known with certainty to belong to a particular species<sup>13</sup>. This uncertainty extends to the OH 7 hand bones, which form part of the holotype of *Homo habilis*<sup>2</sup>, but whose species assignment has been questioned (for example, see ref. 14).

Here we describe a hominin partial skeleton that includes hand and foot bones unambiguously associated with craniodental elements of *P. boisei*. KNM-ER 101000 was recovered in 2019–2021 during survey and excavations at Koobi Fora on the eastern side of Lake Turkana, Kenya (Supplementary Fig. 1). The fossils derive from laminated sandy silt that directly overlies a known hominin trackway surface (FE22)<sup>15</sup>. This

sequence represents a lake margin facies approximately 10 m above the prominent stromatolitic marker bed A6 and 7.6 m below the base of the Koobi Fora Tuff complex<sup>16</sup> (Fig. 1 and Supplementary Information). On the basis of this information, KNM-ER 101000 is estimated to be slightly older than 1.52 million years.

## Craniodental remains

Between approximately 2 and 1 million years ago (Ma) in eastern Africa, there is evidence of up to four contemporaneous hominin species: *P. boisei*, *H. habilis*, *Homo rudolfensis* and *Homo erectus* (for examples, see refs. 17–19). The teeth of KNM-ER 101000 resemble those of *P. boisei* in size more than those of any *Homo* species. Moreover, they exceed the sizes of *Homo* in all dimensions of the mandibular premolars and molars except for the buccolingual breadth of the second lower molar (M<sub>2</sub>), which falls within the upper limits of the early *Homo* range (Extended Data Fig. 2a–f and Supplementary Table 2). In terms of relative proportions, the ratio of the maxillary crown sizes of the canine and third upper molar (M<sup>3</sup>) (55%) of KNM-ER 101000 is within

<sup>1</sup>Department of Anthropology, Stony Brook University, Stony Brook, NY, USA. <sup>2</sup>Turkana Basin Institute, Stony Brook University, Stony Brook, NY, USA. <sup>3</sup>Department of Cell and Developmental Biology, School of Medicine, University of Colorado Anschutz Medical Campus, Aurora, CO, USA. <sup>4</sup>Department of Anthropology, University of Colorado Denver, Denver, CO, USA. <sup>5</sup>Department of Anthropology, Lakehead University, Thunder Bay, Ontario, Canada. <sup>6</sup>Human Origins Program, Department of Anthropology, National Museum of Natural History, Smithsonian Institution, Washington, DC, USA. <sup>7</sup>Australian Research Council Centre of Excellence for Australian Biodiversity and Heritage, University of Wollongong, Wollongong, New South Wales, Australia. <sup>8</sup>Department of Anthropology, Washington University in St Louis, St Louis, MO, USA. <sup>9</sup>Department of Anatomical Sciences, Stony Brook University, Stony Brook, NY, USA. <sup>10</sup>Department of Earth and Planetary Sciences, Rutgers University, Piscataway, NJ, USA. <sup>11</sup>Department of Anthropology, Rutgers University, Piscataway, NJ, USA. <sup>12</sup>Division of Integrative Anatomical Sciences, Department of Medical Education, Keck School of Medicine of USC, Los Angeles, CA, USA. <sup>13</sup>Division of Anthropology, American Museum of Natural History, New York, NY, USA. <sup>14</sup>Research Group 3D Innovation, Stellenbosch University, Matieland, South Africa. <sup>15</sup>Math2Market Inc, Atlanta, GA, USA. <sup>16</sup>Turkana Basin Institute, Nairobi, Kenya. <sup>17</sup>Koobi Fora Research Project, Nairobi, Kenya. <sup>18</sup>Department of Earth Sciences, National Museums of Kenya, Nairobi, Kenya. ✉e-mail: [carrie.mongle@stonybrook.edu](mailto:carrie.mongle@stonybrook.edu)

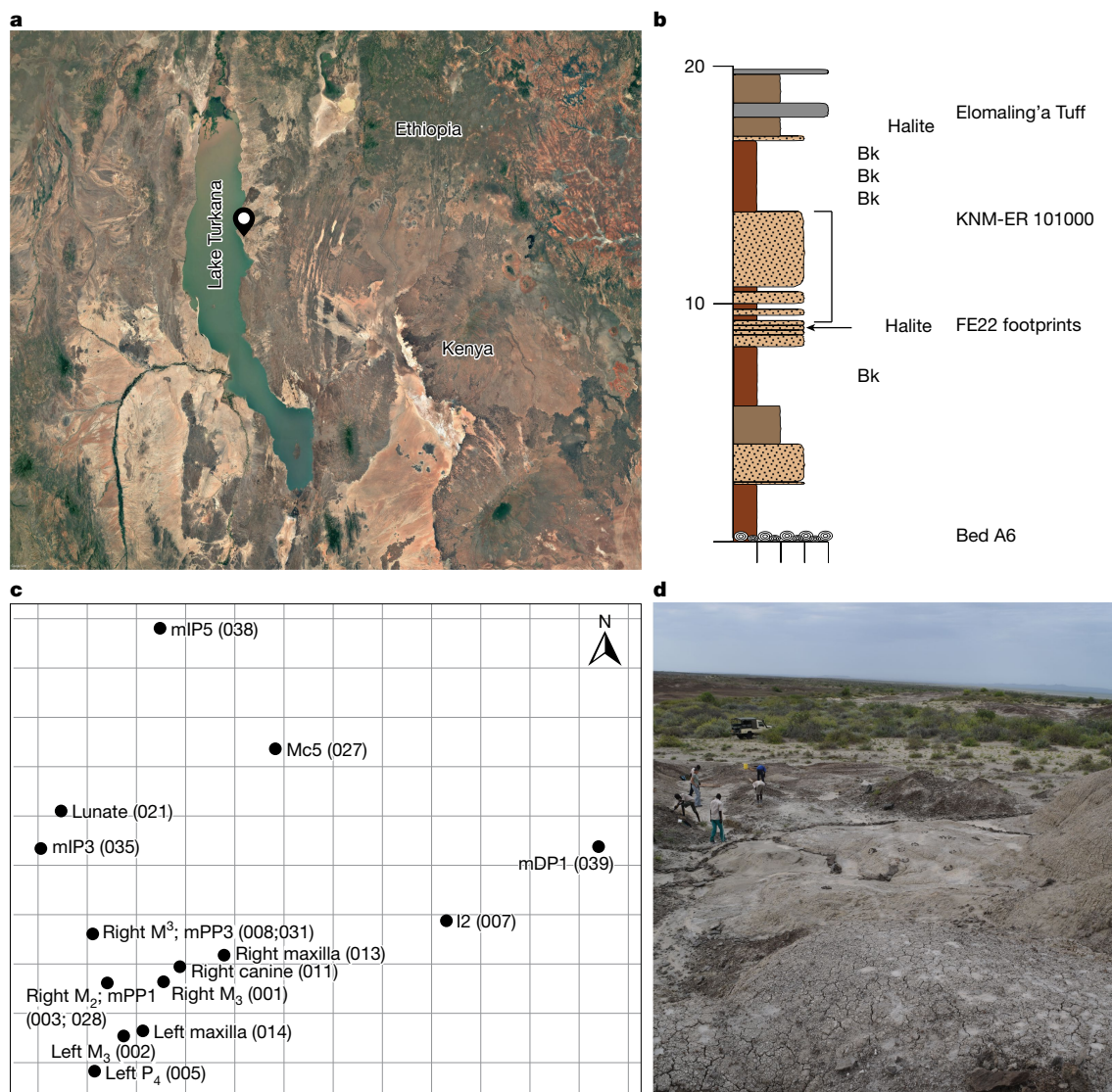


**Fig. 1 | KNM-ER101000 locality, geostratigraphy and specimen distribution map.** **a**, Satellite map of the Turkana Basin region indicating the geospatial location of the KNM-ER 101000 excavation site. **b**, Stratigraphical section of the lake margin facies, including the interval from which the KNM-ER101000 fossils derive. Fine sands with abundant nondecalcified molluscs, silts with saline crusts (halite) and clays with multiple pedogenic carbonate (Bk) horizons characterize this interval of strata. Note that the source strata for KNM-ER 101000 are 10–25 cm above a siltstone layer that has a known hominin trackway

surface (FE22)<sup>15</sup>. **c**, Specimen distribution map of the KNM-ER101000 excavation. Each grid square represents 1 × 1 metre. Numbers in parentheses refer to the specimen numbers in Supplementary Table 1. Specimens not listed on the map were recovered from sieving fragments from the mapped area after excavation. **d**, Image of the outcrop of the excavation site of KNM-ER101000. The photograph was taken from the top of the hill looking down on the site, facing south. Base map in **a** from Google Earth (Google, Landsat/Copernicus, Data SIO, NOAA, US Navy, NGA, GEBCO). Diagram in **b** adapted with permission from ref. 15, AAAS.

the range for *P. boisei* (49–56%) and below that of early *Homo* (66–76%), which signifies that KNM-ER 101000 possessed the relatively small canines that are characteristic of *P. boisei* (Fig. 2b). Hyperthick enamel is another well-established synapomorphy of *Paranthropus*<sup>20–22</sup>. The average enamel thickness (AET)<sup>23,24</sup> of the maxillary and mandibular M3 specimens of KNM-ER101000 is within the *P. boisei* range (M<sub>3</sub>AET = 2.86 and M<sup>3</sup> AET = 2.68; Fig. 2c). Overall, the dentition of KNM-ER 101000 strongly supports its taxonomic attribution to *P. boisei*.

Associated cranial fragments also preserve morphology diagnostic of *P. boisei* (Fig. 2a). These include a parietal fragment that preserves a prominent sagittal crest, which suggests that it can be attributed to a male *P. boisei* individual. The anterior margin of the zygomatic process of the maxilla originates in alignment with the third upper premolar (P<sup>3</sup>)<sup>19,25,26</sup>. Likewise, the nasoalveolar contour of the maxilla is flat, suggesting that the incisors would not have protruded beyond the bicanine line<sup>27</sup>. Computed tomography imaging of this maxillary

fragment revealed a three-rooted fourth premolar (P<sup>4</sup>) (Supplementary Fig. 2), which is universally expressed in *Paranthropus*<sup>28</sup>. However, it is also present in some specimens attributed to early *Homo*. The right temporal bone preserves a well-defined and robust articular eminence, with a maximum preserved mediolateral length of 39 mm, which distinguishes it from the narrower mandibular fossae of *Homo*<sup>25,29</sup>. These features of the maxillary and temporal fragments are congruent with the identification of KNM-ER 101000 as *P. boisei*.

## Hand and wrist elements

Spatially associated with these *P. boisei* craniodental elements are multiple bones from the right and left hands (Fig. 3 and Extended Data Fig. 1). As with the craniodental remains, there is no indication that more than one individual is represented (for example, there is no duplication of elements and no notable difference in element size). Bones of the left

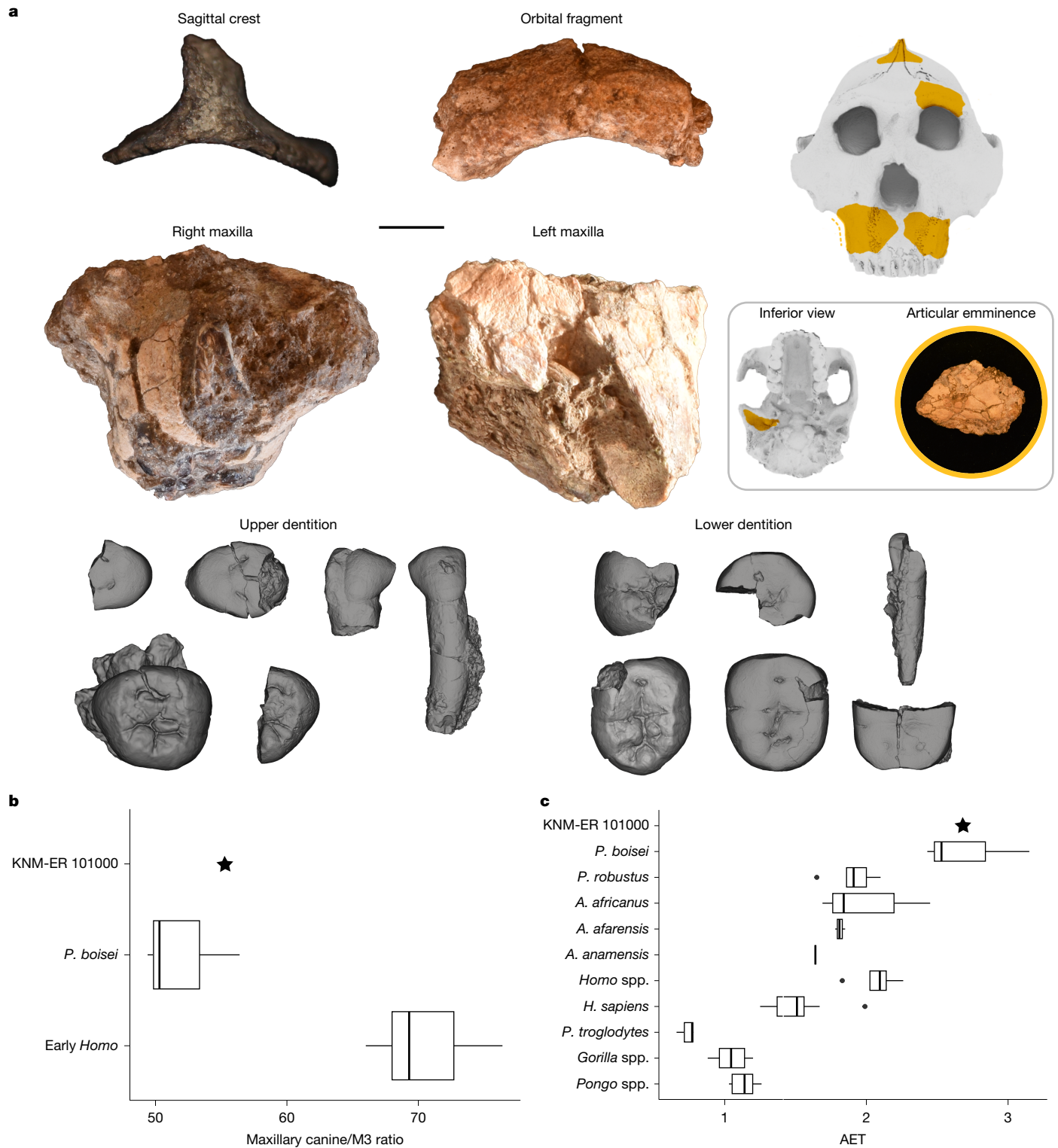


**Fig. 2 | KNM-ER 101000 craniodental remains.** **a**, Diagnostic craniodental elements of KNM-ER 101000 shown in anatomical position against a silhouette of the reconstructed OH 5 cranium. The articular eminence is not to scale. Scale bar, 10 mm. **b**, Comparison of hominin anterior to posterior dentition sizes, depicted here as the ratio of maxillary M3 and canine crown modules, defined as (mesiodistal + buccolingual)/2.  $n = 10$ ; see Supplementary Table 6 for details.

**c**, AET of the maxillary M3 plotted in comparison to hominin and ape data from ref. 23 ( $n = 50$ , see Supplementary Table 4 for details). In **b** and **c**, data are presented as boxplots, with the median indicated by a vertical line, the box spanning the interquartile range and the whiskers extending to  $1.5 \times$  the interquartile range from each quartile. The skull silhouette in **a** was created by Mark Belan.

thumb include a mostly complete manual distal phalanx (mDP1), the proximal end of a proximal phalanx (mPP1) and the proximal half of a first metacarpal (Mc1). The palm is represented by a complete right fifth metacarpal (Mc5) and three other metacarpal shaft fragments.

The finger bones include nine phalanges (six proximal and three intermediate), with the second proximal phalanx (mPP2) and the probable third intermediate (mIP3) phalanx preserved largely intact. Substantial portions of what are provisionally assigned to mIP2 and mPP4 are also

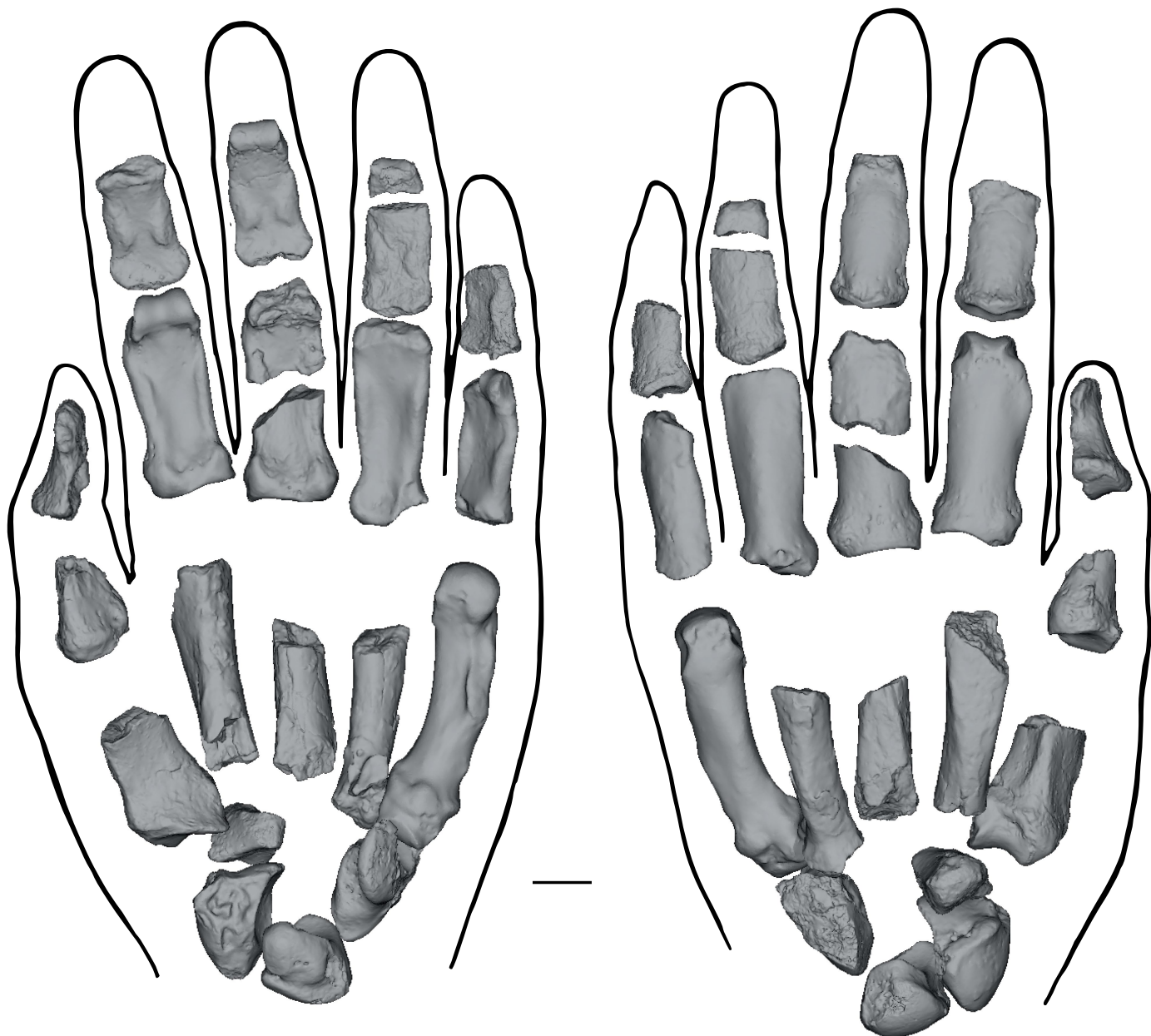


**Fig. 3 | Reconstructed left hand of KNM-ER 101000.** Palmar (left) and dorsal (right) views. The following right elements were mirrored: hamate, lunate, Mc5 and proximal phalanx (second ray). See Supplementary Table 1 for a full list of element attributions and sides (where known). The outline is for illustrative

purposes only and not an interpretation of the relative phalangeal lengths (see Extended Data Fig. 3 and Supplementary Fig. 3 for analyses of digit proportions). Scale bar, 10 mm. The hand outline was created by Francis Tre Lawrence.

preserved along with smaller phalangeal fragments, which are probably mPP3, mPP5 and mIP4. The wrist is represented by the left trapezoid and scaphoid and by the right lunate and hamate.

KNM-ER 101000 indicates that *P. boisei* had essentially modern human-like intrinsic hand proportions. That is, the thumb was long relative to the palm and other fingers (Extended Data Fig. 3a–c and Supplementary Table 3), a characteristic also exhibited by known species of *Australopithecus* but not *Ardipithecus ramidus*, which had more ape-like hand proportions. Although only the base of the mPP1 is preserved, human-like thumb-to-finger proportions are indicated on the basis of the length of the Mc5 against both a reconstruction of the total pollical phalangeal length (using the mDP1 length plus the predicted mPP1 length based on the hallucal proximal phalanx length) and the mDP1 length alone (Supplementary Fig. 3a). Furthermore, the length of mPP2 compared with that of mDP1 indicates a thumb that

was long relative to the index finger, as in recent humans and all fossil hominins except *Ar. ramidus* (Supplementary Fig. 3b). Such proportions in KNM-ER 101000 would have enabled *P. boisei* to form human-like precision grips that require opposition of the distal pads of the fingers to that of the thumb<sup>30</sup>.

The mDP1 is broadly similar in morphology to those of most other early hominin specimens but larger in absolute maximum length and width (Extended Data Fig. 3b). It is very robust, with an expanded apical tuft and a deep proximopalmar fossa and pronounced insertion gable for the tendon of flexor pollicis longus. Weathering prevents full assessment of the unguis fossa, but it seems to have been expansive, which is indicative of a well-developed digital pulp. The exceptionally broad apical tuft of KNM-ER 101000 is most similar to that of OH 7 (but OH 7 lacks any clear indication of a well-developed flexor pollicis longus muscle<sup>30</sup>), as well as to specimens of *Homo naledi* and to Neanderthals.

Earlier hominins such as *Orrorin tugenensis* and *Australopithecus afarensis* exhibit moderately broad tufts similar to recent humans, whereas *Ar. ramidus* resembles *Pan* and *Gorilla* in the narrowness of its tuft. Broadening of the pollical distal phalanx may represent an adaptation to increased manual dexterity (for example, human-like forceful precision grips). However, what drove the extreme broadening of the distal phalanx in some of these hominin species is unclear.

In contrast to species of *Australopithecus*, KNM-ER 101000 exhibits a robust thumb, with evidence of well-developed thenar musculature. The pollical metacarpal, although lacking the distal half, is exceptionally robust with marked entheses. It is considerably larger in relative and absolute size than any of those known for australopithecids, including KNM-ER 47000 (a specimen that has been tentatively attributed to *P. boisei*<sup>31</sup>; Extended Data Fig. 4a and Supplementary Table 3). The articular facet for the trapezium is strongly curved dorsopalmarly and radioulnarly as seen in extant great apes and in *Australopithecus* (Extended Data Fig. 4b,c). Such marked articular curvature is unlike the derived, relatively flatter condition (especially radioulnarly) shared among modern humans, Neanderthals and *H. naledi*.

The trapezoid is well preserved and, similar to those of extant great apes, is wedge-shaped with a relatively large triangular-shaped facet for the scaphoid and a mostly dorsally placed facet for the capitate. The palmar aspect of the bone is expanded proximodistally such that the radial and ulnar portions of the second metacarpal facet are oriented more parallel to the scaphoid facet than is typically seen in extant great apes. However, the palmar portion is not radioulnarly expanded as it is in modern humans, Neanderthals and *H. naledi* (Extended Data Fig. 5a,d).

The scaphoid preserves facets for the radius, capitate, lunate and trapezoid that are all mostly intact, but with some erosion near their respective boundaries; however, the tubercle (and most of the trapezium facet) is missing. As with all hominins and the African apes, the centrale portion is completely incorporated into the body. The shape and orientation of the capitate and lunate facets, as well as the large facet for the trapezoid that distally closes the scaphoid–capitate joint, are most similar to those of extant African apes. By contrast, modern humans, Neanderthals and *H. naledi* display a configuration which is more open distally and is confluent with an enlarged and palmarly placed capitate–trapezoid joint (Extended Data Fig. 5b,e).

The lunate is well preserved. The facet for the capitate head is deeply concave and the radiocarpal surface is convex and mediolaterally broad (Extended Data Fig. 5f). Overall, the lunate exhibits the morphology shared by African apes and hominins. However, in combination, the morphologies of the lunate and scaphoid suggest that KNM-ER 101000 mostly retained a primitive, African ape-like radiocarpal and midcarpal joint configuration (Extended Data Fig. 5c).

As with the thumb, the hypothenar elements of KNM-ER 101000 are robustly developed, which is suggestive of considerable ulnar-side hand strength (Extended Data Fig. 6). The hamulus of the hamate is long relative to the length of the hamate body (Extended Data Fig. 6a,c), which resembles the condition in *Gorilla* (particularly *Gorilla beringei*). However, unlike in *Gorilla*, *Pan* and *Pongo*, KNM-ER 101000 shows a more hominin-like relationship between the hamulus breadth and width and only a moderate distal inclination of the hamulus, which is similar to most other early hominins (Supplementary Fig. 4a,b, measurements are defined in the caption). The large hamulus of KNM-ER 101000 probably provided expanded entheses and increased leverage (longer moment arm) for the opponens digiti minimi and flexor digiti minimi muscles and probably the flexor carpi ulnaris with its connection to the hamulus through the pisohamate ligament. The morphology of the hamulus is accompanied by an Mc5 shaft that is very robust (Extended Data Fig. 6b,c) and exhibits marked radioulnar bowing with an exceptionally large and rugose crest along its ulnar aspect, which marks the distal attachment of the opponens digiti minimi (Extended Data Fig. 6c). In these aspects, the hypothenar complex of KNM-ER

101000 converges on the condition seen in *G. beringei* (Extended Data Fig. 6c). However, *Gorilla* and other great apes tend to have Mc5 and Mc4 bases that are ‘locked in’ by the strong distal inclination of the hamulus. By contrast, KNM-ER 101000 exhibits a more convex surface on the Mc5, and the correspondingly concave surface on the hamate indicates increased mobility of the fifth ray, similar to that of recent humans and other hominins. Pronounced protuberances at the base of the Mc5 mark attachment of the extensor carpi ulnaris (on the dorsal side) and the flexor carpi ulnaris (on the palmar side by way of the pisometacarpal ligament) along with the capsular ligaments of the fifth carpometacarpal joint.

The morphology of the non-pollical phalanges is consistent with that of the thumb and hypothenar region in exhibiting marked robusticity (Extended Data Figs. 7 and 8). The complete mPP2 is the most robust specimen in the fossil comparative sample. Moreover, its exceptional radioulnar breadth at the midshaft relative to the proximodistal length is matched only by a few male specimens of *Gorilla* (Extended Data Fig. 7a). KNM-ER 47000 (ref. 31) (ostensibly also representing *P. boisei*) is considerably more gracile, although this difference could reflect sexual dimorphism (see the *G. beringei* male–female comparison in Extended Data Fig. 7b). In overall gestalt, the proximal phalanges of KNM-ER 101000 resemble those of gorillas (especially *G. beringei*), although the complete mPP2 lacks strong longitudinal shaft curvature (Extended Data Fig. 7c,d) as do the less complete phalanges from the other digits (based on qualitative assessments). This result suggests that climbing and suspension may not have been a regular component of the adult male *P. boisei* locomotor repertoire. All of the mPP specimens of KNM-ER 101000 are similar to those of gorillas in having pronounced flexor sheath ridges, which indicate strong recruitment of the long digital flexors (sometimes interpreted as another correlate of climbing or suspension). However, these ridges are generally less well developed in the more arboreal great apes (genera *Pongo* and *Pan*), which renders the biological role of this trait (beyond strong digital grasping) difficult to interpret<sup>32–35</sup>.

The intermediate phalanges of KNM-ER 101000 evince a robusticity similar to the proximal phalanges, which is again matched only by a few *Gorilla* specimens and by OH 7, possible *P. robustus* or *Homo* specimens from Swartkrans and some Neanderthal specimens. The longitudinal shaft curvature of the intermediate phalanges does not clearly separate recent *Homo sapiens* from the African apes, but the measurable intermediate phalanx of KNM-ER 101000 is among the least curved in the fossil sample, with only two specimens from Swartkrans exhibiting lower included angle values (Supplementary Table 5). Relative to the midshaft radioulnar width, the mPP2 of KNM-ER 101000 has an exceptionally narrow distal trochlea (Extended Data Fig. 8b). Although relative trochlear breadth has been suggested to align OH 7 with *Paranthropus*<sup>14</sup> (rather than its typical attribution to *H. habilis*<sup>36</sup>), there is extensive overlap with the extant ape sample and several of the other hominin samples in this measurement (Extended Data Fig. 8b).

A small fragment of the left proximal radius of KNM-ER 101000 is preserved. Much like the other known radius of *P. boisei* (OH 80)<sup>37</sup>, the size of the radial tuberosity (long axis of enthesis = 27.8 mm, perpendicular to the long axis = 17.6 mm) suggests that KNM-ER 101000 possessed a large biceps brachii muscle that was probably capable of generating strong forearm flexion and supination. Its absolute cross-sectional cortical area is within the range of *Gorilla* and in the upper quartile of *Pan troglodytes*, well above that of recent humans (Supplementary Fig. 5). Some studies have suggested that *P. boisei* would have engaged in arboreal behaviours on the basis of the thick cortical bone observed in the tentatively attributed humerus of KNM-ER 47000 (ref. 38). Although a strong upper limb could have facilitated climbing behaviours, other explanations such as systemically thick cortical bone in this species should also be considered in the context of the overall morphological pattern across the postcranium<sup>39</sup>.

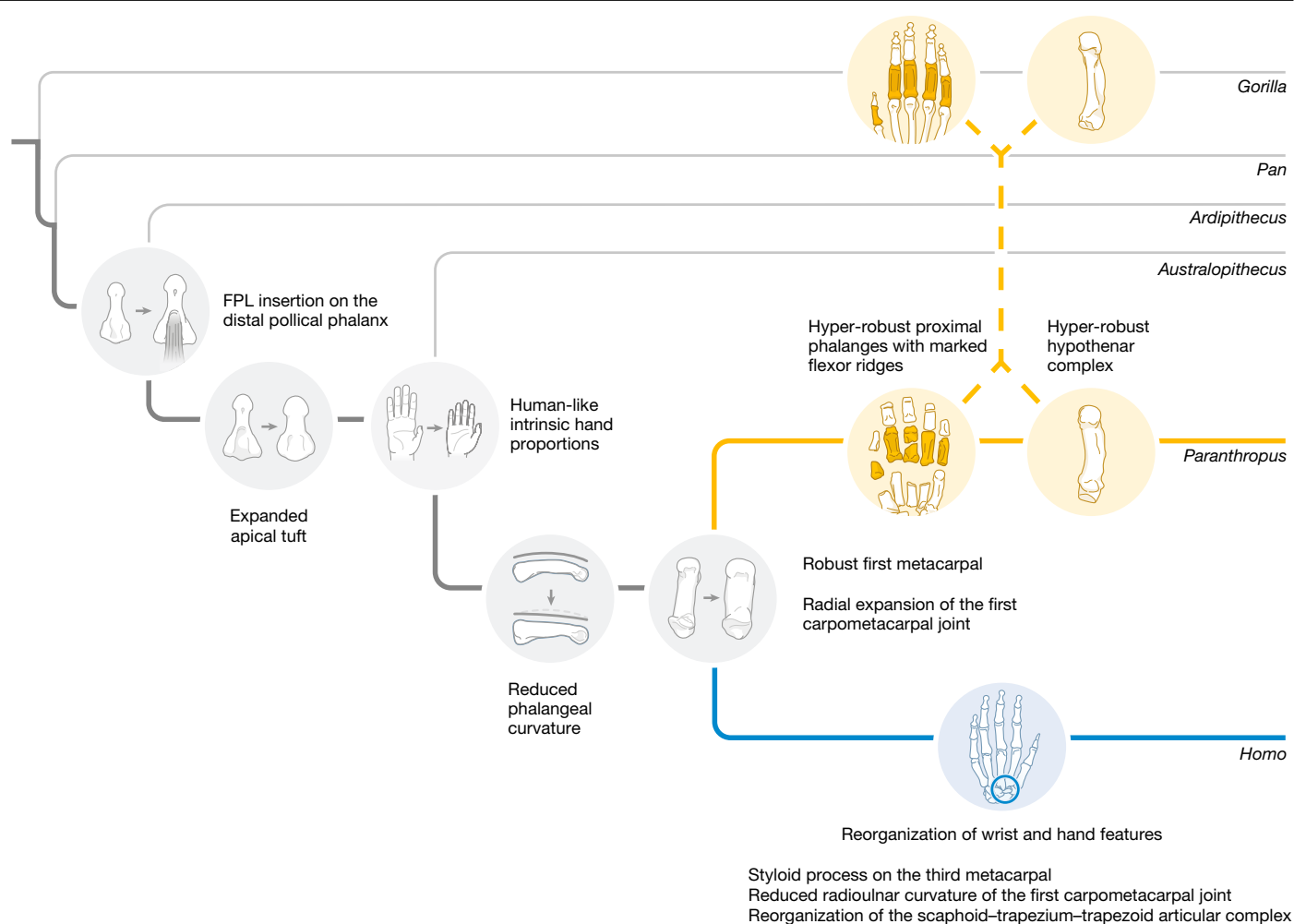


**Fig. 4 | Reconstruction of hominin hand evolution.** Summary of ancestral state reconstructions highlighting key inferred transitions in hominin hand evolution. Ancestral state reconstructions were conducted across a phylogeny consisting of 6 extant apes and 14 hominin fossils for 20 morphological

characteristics using maximum parsimony. No polarity or character ordering was assumed a priori. KNM-ER 101000 was taken as the sole representative of *P. boisei*, although it never differed in character state from KNM-ER 47000. FPL, flexor pollicis longus. Illustrations were created by Mark Belan.

### Pedal elements

The right foot of KNM-ER 101000 is represented by a complete hallucal proximal phalanx (pPP1), a non-hallucal proximal phalanx (probably pPP5) and a right third metatarsal (Mt3) that is missing its distal end (Extended Data Figs. 9 and 10). The pPP1 is intrinsically robust, with a dorsally canted proximal articular surface similar to that of recent humans and other hominin fossils (for example, SKX 45690 and StW 470). Dorsal canting facilitates increased dorsiflexion during bipedal push-off<sup>40,41</sup>. The logged ratio of pPP1-to-pPP5 length in KNM-ER 101000 reflects a hallux that is long relative to that of great apes but short in comparison to recent humans. The pPP5 of KNM-ER 101000 is relatively short, displaying reduced curvature compared to *Ar. ramidus* (ARA-VP-6/500-044 and GWM67/P2u) and *A. afarensis* (A.L. 333-115i, A.L. 333-154 and A.L. 333-160) along with a greater dorsal inclination of its metatarsophalangeal joint facet that matches pedal phalanges from Neanderthals, Pleistocene *H. sapiens* and SKX 16699 (ref. 42), which probably reflect similar functionality of the lateral forefoot (Extended Data Figs. 9 and 10). A high positive Mt3 torsion angle (about 41°) in KNM-ER 101000 indicates the presence of a well-developed transverse arch, which significantly contributes to stiffness in the hominin foot<sup>43</sup>. By comparison, the Mt3 of OH 8 has a lower Mt3 torsion angle (15°) than KNM-ER 10100, falling near KNM-ER 803 and Sterkfontein specimens attributed to *Australopithecus africanus*, but its value falls within the

range of the modern human sample. Finally, the Mt3 of KNM-ER 101000 displays a dorsoplantarly tall and relatively flat proximal articular surface, which is associated with tarsometatarsal joint stability in bipeds<sup>44</sup>. The Mt3 base of OH 8 is slightly shorter than that of KNM-ER 101000, with a ratio value falling near those of *H. naledi* (U.W. 101-1035 and U.W. 101-1457), Dmanisi *H. erectus* (D2021) and SKX 247. However, the difference between OH 8 and KNM-ER 101000 could be sampled in our modern human and chimpanzee samples. Overall, the pedal elements of KNM-ER 101000 indicate that increased stiffness and bipedal push-off characterized the foot of *P. boisei*. However, the relatively short hallux of KNM-ER 101000 also suggests that the push-off mechanics in *P. boisei* would have differed slightly from those of recent humans (sensu<sup>45</sup>). The reduced intrinsic length and diaphyseal curvature of its non-hallucal proximal phalanx are more human-like than those of *A. afarensis* and *Ar. ramidus*, which suggests that there was little reliance on pedal grasping in *P. boisei* by approximately 1.5 Ma. Although a fully bipedal foot does not preclude occasional (or even frequent) climbing, as observed in some human populations<sup>46</sup>, it suggests that this behaviour was not the primary selective force in the locomotor repertoire of this species.

### Discussion

It has long been assumed that the earliest members of the genus *Homo* manufactured and used stone tools<sup>2</sup>. However, the discovery

of 3.3 million-year-old stone tools at Lomekwi<sup>47</sup> together with 3.0-million-year-old Oldowan artefacts alongside a purported *Paranthropus* molar at Nyayanga<sup>4</sup> has reignited debate about possible tool use in other taxa. On the basis of analyses of KNM-ER 101000, it is clear that the hand of *P. boisei* had derived thumb–finger length proportions and was probably capable of grips similar to those of modern humans. However, judging from the retention of a suite of plesiomorphic features in the wrist and base of the thumb, radioulnar transmission of loads from the powerful thumb probably differed from that of recent humans and Neanderthals, which indicate differences in habitual thumb use during manual manipulation. We propose that precision-pinch-type grips were likely to be less effective in *P. boisei* than in later members of the genus *Homo* with a more derived trapeziometacarpal and radial wrist morphology. However, this does not rule out tool behaviours (including the making and use of early lithic technology).

Overall, the functional morphology of the hand and wrist of KNM-ER 101000 suggests that it had a powerful grip strength, particularly in the ulnar aspect of the hand. An important caveat is that tool use may not have been the only factor driving selection on hominin hands. For example, in some fossil hominin taxa such as *A. afarensis* and *H. naledi*, there is compelling evidence to suggest that climbing was an important part of the locomotor repertoire. There are indications of strong grasping in KNM-ER 101000 that would have facilitated climbing performance, and *P. boisei* may have engaged in arboreal behaviour at some frequency. However, one of the clearest signals of frequent climbing and suspensory behaviour in primates (that is, longitudinal shaft curvature of the manual and pedal phalanges<sup>48</sup>) is notably less expressed in KNM-ER 101000 than in *A. afarensis*, *H. naledi* and extant African apes, whereas pedal morphology in KNM-ER 101000 evinces a greater commitment to terrestriality than in earlier hominins.

Although one possibility for explaining the convergence of gorilla-like hand morphology in *P. boisei* is that it may have adopted a climbing style that was specifically gorilla-like, the distinctive features of the climbing gait in gorillas seem to be a compensation for their large body mass<sup>49</sup>. Thus, it is unclear why *P. boisei* would have adopted such a mode of climbing given that estimates of its body mass<sup>50</sup> are similar to those of other early hominins such as *A. afarensis*<sup>51</sup>, and notably smaller than modern gorillas. Consequently, although any primate will use its hands in a variety of behaviours, climbing competency may not have been the sole (nor likely to be the primary) selective factor in the convergent evolution of the gorilla-like manual features in *P. boisei*.

In primates more broadly, feeding behaviours often require complex manual manipulation and forceful processing<sup>52</sup>. Mountain gorillas use forceful, palm dominated power grasping that incorporates the fifth digit during arboreal behaviours, but they also regularly use their hands in this capacity to access edible portions of tough vegetation<sup>53</sup>. The morphological convergence of *P. boisei* hand morphology with that of *G. beringei* (especially in the hypothenar region and manual phalanges) is notable in light of dietary reconstructions indicating that *P. boisei* subsisted on a tough diet dominated by herbaceous, grass-like plants (reviewed in ref. 54). On the basis of the overall morphology of the postcranial elements of KNM-ER 101000 (and possibly other specimens attributed to *P. boisei*, such as OH 80), the similarities to gorillas may reflect intensive manual processing of such plants for food.

In addition to insights into the paleobiology of *Paranthropus*, KNM-ER 101000 provides an opportunity to revisit longstanding debates over the taxonomic attribution of the foot bones from OH 7 and the hand bones from OH 8 (refs. 10,14,55). The morphology and relative proportions of the intermediate phalanges of KNM-ER 101000 are highly similar to those of OH 7. Although this similarity could be viewed as evidence in favour of the hypothesis that the hand of OH 7 belongs to *Paranthropus* rather than *H. habilis*<sup>14</sup>, the degree of variation in relative trochlear breadth makes the taxonomic significance of this metric unclear. It seems unlikely that a pollical metacarpal base as curved as the Mc1 in KNM-ER 101000 (or KNM-ER 47000) would articulate with

a trapezium like in OH 7. This finding weakens the hypothesis that the hand of OH 7 belongs to *Paranthropus*<sup>14</sup> (further detailed analyses are required to establish whether this range of variation occurs in a single species). Poor scaphoid preservation in both OH 7 and KNM-ER 101000 limits the utility of comparison between these elements. The Mt3 of KNM-ER 101000 is similar to that of OH 8, which has intrinsically large Mt2 and Mt4 articular facets and a dorsoplantarily tall diaphysis relative to its mediolateral breadth. By contrast, the Mt3 diaphysis of KNM-ER 101000 has a substantially greater transverse curvature and a dorsoplantarily flatter proximal articular surface than OH 8. However, the extent to which these metatarsal traits distinguish *P. boisei* from *H. habilis* is currently unknown.

More generally, because *Homo* and *Paranthropus* are sister taxa<sup>21,22,27</sup>, the KNM-ER 101000 fossils enable the reconstruction of the probable ancestral condition of the hand that would have characterized the earliest members of both the *Homo* and *Paranthropus* lineages. Modern humans and Neanderthals share several derived features in the thumb and radial wrist bones that probably evolved as an adaptation to making and using stone tools<sup>3,7,56–58</sup>. Exactly when this complex of derived features first evolved remains unclear, but available fossil evidence suggests that it had occurred by at least 1.4 Ma (for example, KNM-WT 51260)<sup>59</sup>.

Our analyses reveal that the last common ancestor (LCA) of *Homo* and *Paranthropus* (and therefore the earliest members of the genus *Homo*) would have possessed a relatively robust Mc5 and Mc1 and a radially expanded first carpometacarpal joint (Fig. 4). This proportional increase in the marginal elements of the hand represents an adaptive shift from earlier australopiths, such as those probably responsible for the Lomekwian stone tools<sup>47</sup>, and indicates an increased reliance on stabilized power grips<sup>56</sup>. By comparison, derived aspects of the modern human wrist that facilitate effective precision-pinch grips do not seem to have been present in the *Homo–Paranthropus* LCA. Rather, these evolved later in the *Homo* lineage.

If the derived features of the *P. boisei* hand are indeed convergent with gorillas to facilitate strong and repeated grips involved in intensive food processing, then it may support a model in which *Paranthropus* and *Homo* evolved divergent dietary strategies in a sympatric setting that allowed them to subsist as ecological specialists and generalists, respectively, with *Homo* including further commitment to intensified tool use<sup>60</sup>.

## Online content

Any methods, additional references, Nature Portfolio reporting summaries, source data, extended data, supplementary information, acknowledgements, peer review information; details of author contributions and competing interests; and statements of data and code availability are available at <https://doi.org/10.1038/s41586-025-09594-8>.

1. Leakey, L. B. New fossil skull from Olduvai. *Nature* **184**, 491–493 (1959).
2. Leakey, L. B., Tobias, P. V. & Napier, J. R. A new species of the genus *Homo* from the Olduvai Gorge. *Nature* **202**, 7–9 (1964).
3. Tocheri, M. W., Orr, C. M., Jacobsky, M. C. & Marzke, M. W. The evolutionary history of the hominin hand since the last common ancestor of *Pan* and *Homo*. *J. Anat.* **212**, 544–562 (2008).
4. Plummer, T. W. et al. Expanded geographic distribution and dietary strategies of the earliest Oldowan hominins and *Paranthropus*. *Science* **379**, 561–566 (2023).
5. Wood, B. A. & Richmond, B. G. Human evolution: taxonomy and paleobiology. *J. Anat.* **196**, 19–60 (2000).
6. Panger, M. A., Brooks, A. S., Richmond, B. G. & Wood, B. Older than the Oldowan? Rethinking the emergence of hominin tool use. *Evol. Anthropol.* **11**, 235–245 (2002).
7. Tocheri, M. W. et al. The primitive wrist of *Homo floresiensis* and its implications for hominin evolution. *Science* **317**, 1743–1745 (2007).
8. Susman, R. L. Hand of *Paranthropus robustus* from Member 1, Swartkrans: fossil evidence for tool behavior. *Science* **240**, 781–784 (1988).
9. Susman, R. L. New hominid fossils from the Swartkrans formation (1979–1986 excavations): postcranial specimens. *Am. J. Phys. Anthropol.* **79**, 451–474 (1989).
10. Susman, R. L. Fossil evidence for early hominid tool use. *Science* **265**, 1570–1573 (1994).
11. Susman, R. L. Response: thumbs, tools, and early humans. *Science* **268**, 589 (1995).

12. Trinkaus, E. & Long, J. C. Species attribution of the Swartkrans Member 1 first metacarpals: SK 84 and SKX 5020. *Am. J. Phys. Anthropol.* **83**, 419–424 (1990).
13. Grine, F. E., Mongle, C. S., Fleagle, J. G. & Hammond, A. S. The taxonomic attribution of African hominin postcrania from the Miocene through the Pleistocene: associations and assumptions. *J. Hum. Evol.* **173**, 103255 (2022).
14. Moyà-Solà, S., Kohler, M., Alba, D. M. & Almécija, S. Taxonomic attribution of the Olduvai hominid 7 manual remains and the functional interpretation of hand morphology in robust australopithecines. *Folia Primatol.* **79**, 215–250 (2008).
15. Hatala, K. G. et al. Footprint evidence for locomotor diversity and shared habitats among early Pleistocene hominins. *Science* **386**, 1004–1010 (2024).
16. Brown, F. H. & Feibel, C. S. Revision of lithostratigraphic nomenclature in the Koobi Fora region, Kenya. *J. Geol. Soc.* **143**, 297–310 (1986).
17. Leakey, M. G. et al. New fossils from Koobi Fora in northern Kenya confirm taxonomic diversity in early *Homo*. *Nature* **488**, 201–204 (2012).
18. Neubauer, S. et al. Reconstruction, endocranial form and taxonomic affinity of the early *Homo calvaria* KNM-ER 42700. *J. Hum. Evol.* **121**, 25–39 (2018).
19. Wood, B. A. *Hominid Cranial Remains. Koobi Fora Research Project* Vol. 4 (Oxford Univ. Press, 1991).
20. Martin, L. B., Boyde, A. & Grine, F. E. Enamel structure in primates: a review of scanning electron microscope studies. *Scanning Microsc.* **2**, 1503–1526 (1988).
21. Mongle, C. S., Strait, D. S. & Grine, F. E. Expanded character sampling underscores phylogenetic stability of *Ardipithecus ramidus* as a basal hominin. *J. Hum. Evol.* **131**, 28–39 (2019).
22. Mongle, C. S., Strait, D. S. & Grine, F. E. An updated analysis of hominin phylogeny with an emphasis on re-evaluating the phylogenetic relationships of *Australopithecus sediba*. *J. Hum. Evol.* **175**, 103311 (2023).
23. Lockey, A. L., Alemseged, Z., Hublin, J.-J. & Skinner, M. M. Maxillary molar enamel thickness of Plio-Pleistocene hominins. *J. Hum. Evol.* **142**, 102731 (2020).
24. Skinner, M. M., Alemseged, Z., Gounis, C. & Hublin, J.-J. Enamel thickness trends in Plio-Pleistocene hominin mandibular molars. *J. Hum. Evol.* **85**, 35–45 (2015).
25. Tobias, P. V. *The Cranium and Maxillary Dentition of Australopithecus (Zinjanthropus) Boisei*. Vol. 2, Olduvai Gorge (Cambridge Univ. Press, 1967).
26. Rak, Y. Y. *The Australopithecine Face* (Academic, 1983).
27. Strait, D. S., Grine, F. E. & Moniz, M. A. A reappraisal of early hominid phylogeny. *J. Hum. Evol.* **32**, 17–82 (1997).
28. Wood, B. A. & Engleman, C. A. Analysis of the dental morphology of Plio-Pleistocene hominids. V. Maxillary postcanine tooth morphology. *J. Anat.* **161**, 1–35 (1988).
29. Kimbel, W. H., White, T. D. & Johanson, D. C. Cranial morphology of *Australopithecus afarensis*: a comparative study based on a composite reconstruction of the adult skull. *Am. J. Phys. Anthropol.* **64**, 337–388 (1984).
30. Almécija, S., Moyà-Solà, S. & Alba, D. M. Early origin for human-like precision grasping: a comparative study of pollical distal phalanges in fossil hominins. *PLoS ONE* **5**, e11727 (2010).
31. Richmond, B. G. et al. The upper limb of *Paranthropus boisei* from Ileret, Kenya. *J. Hum. Evol.* **141**, 102727 (2020).
32. Susman, R. L. Comparative and functional morphology of hominoid fingers. *Am. J. Phys. Anthropol.* **50**, 215–236 (1979).
33. Bucchi, A., Luengo, J., Del Bove, A. & Lorenzo, C. Insertion sites in manual proximal phalanges of African apes and modern humans. *Am. J. Phys. Anthropol.* **173**, 556–567 (2020).
34. Syeda, S. M., Tsegai, Z. J., Cazenave, M., Skinner, M. M. & Kivell, T. L. Cortical bone architecture of hominid intermediate phalanges reveals functional signals of locomotion and manipulation. *Am. J. Biol. Anthropol.* **184**, e24902 (2024).
35. Syeda, S. M., Tsegai, Z. J., Cazenave, M., Skinner, M. M. & Kivell, T. L. Cortical bone distribution of the proximal phalanges in great apes: implications for reconstructing manual behaviours. *J. Anat.* **243**, 707–728 (2023).
36. Susman, R. L. & Stern, J. T. Functional morphology of *Homo habilis*. *Science* **217**, 931–934 (1982).
37. Domínguez-Rodrigo, M. et al. First partial skeleton of a 1.34-million-year-old *Paranthropus boisei* from Bed II, Olduvai Gorge, Tanzania. *PLoS ONE* **8**, e80347 (2013).
38. Lague, M. R. et al. Humeral anatomy of the KNM-ER 47000 upper limb skeleton from Ileret, Kenya: implications for taxonomic identification. *J. Hum. Evol.* **126**, 24–38 (2019).
39. Baab, K. L., Copes, L. E., Ward, D. L., Wells, N. & Grine, F. E. Using modern human cortical bone distribution to test the systemic robusticity hypothesis. *J. Hum. Evol.* **119**, 64–82 (2018).
40. Latimer, B. & Lovejoy, C. O. Metatarsophalangeal joints of *Australopithecus afarensis*. *Am. J. Phys. Anthropol.* **83**, 13–23 (1990).
41. Fernández, P. J. et al. Evolution and function of the hominin forefoot. *Proc. Natl Acad. Sci. USA* **131**, 8746–8751 (2018).
42. Trinkaus, E. & Patel, B. A. An Early Pleistocene human pedal phalanx from Swartkrans, SKX 16699, and the antiquity of the human lateral forefoot. *C. R. Palevol* **15**, 978–987 (2016).
43. Venkadesan, M. et al. Stiffness of the human foot and evolution of the transverse arch. *Nature* **579**, 97–100 (2020).
44. DeSilva, J., McNutt, E., Benoit, J. & Zipfel, B. One small step: a review of Plio-Pleistocene hominin foot evolution. *Am. J. Phys. Anthropol.* **168**, 63–140 (2019).
45. Susman, R. L. & Brain, T. M. New first metatarsal (SKX 5017) from Swartkrans and the gait of *Paranthropus robustus*. *Am. J. Phys. Anthropol.* **77**, 7–15 (1988).
46. Venkataraman, V. V., Kraft, T. S. & Dominy, N. J. Tree climbing and human evolution. *Proc. Natl Acad. Sci. USA* **110**, 1237–1242 (2013).
47. Harmand, S. et al. 3.3-million-year-old stone tools from Lomekwi 3, West Turkana, Kenya. *Nature* **521**, 310–315 (2015).
48. Rein, T. R. The correspondence between proximal phalanx morphology and locomotion: implications for inferring the locomotor behavior of fossil catarrhines. *Am. J. Phys. Anthropol.* **146**, 435–445 (2011).
49. Neufuss, J., Robbins, M. M., Baeumer, J., Humle, T. & Kivell, T. L. Gait characteristics of vertical climbing in mountain gorillas and chimpanzees. *J. Zool.* **306**, 129–138 (2018).
50. Ruff, C. B. & Wood, B. A. The estimation and evolution of hominin body mass. *Evol. Anthropol.* **32**, 223–237 (2023).
51. Smith, R. J. & Jungers, W. L. Body mass in comparative primatology. *J. Hum. Evol.* **32**, 523–559 (1997).
52. Marzke, M. in *Stone Knapping: The Necessary Conditions for a Uniquely Hominin Behaviour* (eds Roux V. & Brill, B.) 243–255 (McDonald Institute Monograph, 2006).
53. Neufuss, J., Robbins, M. M., Baeumer, J., Humle, T. & Kivell, T. L. Manual skills for food processing by mountain gorillas (*Gorilla beringei beringe*) in Bwindi Impenetrable National Park, Uganda. *Biol. J. Linn. Soc.* **127**, 543–562 (2019).
54. Sponheimer, M., Daegling, D. J., Ungar, P. S., Bobe, R. & Paine, O. C. C. Problems with *Paranthropus*. *Quat. Int.* **650**, 40–51 (2023).
55. Wood, B. A. Olduvai Bed I post-cranial fossils: a reassessment. *J. Hum. Evol.* **3**, 373–378 (1974).
56. Kivell, T. L. Evidence in hand: recent discoveries and the early evolution of human manual manipulation. *Philos. Trans. R. Soc. Lond. B Biol. Sci.* **370**, 20150105 (2015).
57. Marzke, M. W. et al. Comparative 3D quantitative analyses of trapeziometacarpal joint surface curvatures among living catarrhines and fossil hominins. *Am. J. Phys. Anthropol.* **141**, 38–51 (2010).
58. Lorenzo, C., Arsuaga, J. L. & Carretero, J. M. Hand and foot remains from the Gran Dolina Early Pleistocene site (Sierra de Atapuerca, Spain). *J. Hum. Evol.* **37**, 501–522 (1999).
59. Ward, C. V., Tocheri, M. W., Plavcan, J. M., Brown, F. H. & Manthi, F. K. Early Pleistocene third metacarpal from Kenya and the evolution of modern human-like hand morphology. *Proc. Natl Acad. Sci. USA* **111**, 121–124 (2014).
60. O'Brien, K., Hebdon, N. & Faith, J. T. Paleoeological evidence for environmental specialization in *Paranthropus boisei* compared to early *Homo*. *J. Hum. Evol.* **177**, 103325 (2023).

**Publisher's note** Springer Nature remains neutral with regard to jurisdictional claims in published maps and institutional affiliations.



**Open Access** This article is licensed under a Creative Commons Attribution-NonCommercial-NoDerivatives 4.0 International License, which permits any non-commercial use, sharing, distribution and reproduction in any medium or format, as long as you give appropriate credit to the original author(s) and the source, provide a link to the Creative Commons licence, and indicate if you modified the licensed material. You do not have permission under this licence to share adapted material derived from this article or parts of it. The images or other third party material in this article are included in the article's Creative Commons licence, unless indicated otherwise in a credit line to the material. If material is not included in the article's Creative Commons licence and your intended use is not permitted by statutory regulation or exceeds the permitted use, you will need to obtain permission directly from the copyright holder. To view a copy of this licence, visit <http://creativecommons.org/licenses/by-nc-nd/4.0/>.

© The Author(s) 2025

## Methods

Immediately after specimen excavation and preparation, surface scans of each fossil element were generated by T. Gichunge using a HDI Advance 3D scanner (Polyga). Subsequently, micro-computed tomography (microCT) scans of KNM-ER 101000 were generated at the Stellenbosch University CT Scanner Facility<sup>64</sup> with a General Electric Phoenix VTOMEX L240 microCT system (the scan resolution ranged from 15 to 50  $\mu\text{m}$  depending on the size and density of the element).

### Dental metrics

Linear measurements of the dentition of KNM-ER 101000 were recorded from the original fossils using Mauer 0.05 mm accuracy dial calipers. Comparative dental metrics were obtained from published sources (Supplementary Tables 6–10). For comparisons between the anterior and posterior dentition, crown modules of hominin maxillary M3 specimens and canines were calculated per a previous study<sup>62</sup>.

To measure enamel thickness, buccolingual sections through the apices of the dentine horns of the mesial cusps of the unworn maxillary RM<sup>3</sup> (protocone and paracone) and the unworn mandibular RM<sub>3</sub> (metaconid and protoconid) were virtually extracted from the microCT scans of these teeth in Avizo (v.2021). In each slice, the enamel–dentine junction (EDJ) was clearly visible, and the area ( $\text{mm}^2$ ) of the enamel cap was measured using ImageJ. With reference to the RM<sub>3</sub>, a wedge of dentine was lost below the preserved EDJ of the metaconid, and the missing cervical extension of its enamel cap could be estimated with reasonable accuracy by following its curvature inferiorly as previously advocated<sup>63</sup>. The area of the narrow crack through the cusp tip of the metaconid was subtracted from the overall estimated measurement of the enamel cap to obtain a value of 63.21  $\text{mm}^2$ , and its inferior length was subtracted from the overall estimated length of the EDJ to obtain a value of 22.11 mm. With reference to the RM<sup>3</sup>, the area of the wide crack through the intercuspal embrasure (1.80  $\text{mm}^2$ ) was subtracted from the overall measurement of the enamel cap to obtain a value of 67.70  $\text{mm}^2$ , and its inferior length (0.73 mm) was subtracted from the overall measured length of the EDJ to obtain a value of 25.25 mm. The AET was then calculated by dividing the area of the enamel cap by the length of the EDJ. Summary metrics of comparative data from refs. 23,24 are provided in Supplementary Table 4.

### Linear measurements of metacarpals and phalanges

Relevant linear dimensions of KNM-ER 101000 were measured and compared with data from extant comparative groups and available fossil hominins (see Supplementary Tables 11–37 for details of the compositions of extant and fossil samples and data sources for each analysis).

### Estimation of KNM-ER 101000 mPP1 length

Only the proximal base of the mPP1 is preserved for KNM-ER 101000. To estimate the total pollical phalangeal length (proximal plus distal), the mPP1 length was estimated on the basis of the length of the hallux proximal phalanx, which in the comparative sample of extant *H. sapiens* ( $n = 53$ ), *Pan* spp. ( $n = 52$ ) and *Gorilla* spp. ( $n = 48$ ) specimens correlates strongly with pollical proximal phalanx length (least squares regression:  $\text{mPP1 length} = 0.997 \times \text{pPP1 length} - 0.38$ ;  $r^2 = 0.66$ ;  $P < 0.001$ ). The total mPP1 and mDPI length using the mean estimate of the mPP1 length and the upper and lower 95% prediction intervals are plotted against the Mc5 length in Extended Data Fig. 3a to show the uncertainty, but is human-like in all cases. Note the relative length of only the distal pollical phalanx relative to the Mc5 length. Supplementary Fig. 3 also demonstrates the human-like proportions.

### Manual phalangeal curvature

The longitudinal shaft curvature of the mPP2 and the complete mIP3 of KNM-ER 101000 were quantified using the included angle method. Landmarks were extracted from the 3D polygon model of the specimen

to measure dimensions used to calculate the included angle per a previously described method<sup>64</sup>. The extant comparative sample was measured in the same way along with all compared fossils, except for one whose included angle values were taken from the literature (OH 86)<sup>65</sup>. The sample composition for the curvature analysis is provided in Supplementary Tables 34 and 35.

### First metacarpal proximal articular surface

The principal curvatures of the articular surface were quantified for the Mc1 of KNM-ER 101000 and the extant and fossil comparative samples in the dorsopalmar and radioulnar directions using a quadric surface fit with a least-squares method<sup>67</sup> (Extended Data Fig. 4b). Zero values indicate a flat surface with no curvature, whereas values greater or less than zero indicate a curved surface with more curved surfaces having larger absolute values than less curved surfaces. Because this articular surface in hominids is typically saddle-shaped, the sign indicates the direction of curvature (for example, dorsopalmar is positive, radioulnar is negative). Comparative sample details are provided in Supplementary Tables 21 and 22.

### Trapezoid shape

A canonical variate analysis of trapezoid shape was conducted using angles between articular surfaces and relative surface areas (Extended Data Fig. 5a). The former were quantified by fitting least-squares planes to each and measuring the angles between the resulting planes<sup>66</sup>, whereas the latter were quantified by dividing the articular surface area by the surface area of the entire bone<sup>67</sup>. Comparative sample details are provided in Supplementary Tables 23 and 24.

### Scaphoid shape

A 3D geometric morphometric analysis of the preserved portions of the scaphoid of KNM-ER 101000 was conducted (Extended Data Fig. 5b). Using Stratovan Checkpoint software, surface patches were fit to the radius and capitate articular facets and to the preserved portion of the trapezium–trapezoid facet. Landmark patches (density of  $9 \times 9$ ) were manually placed using the ‘patches’ option in Stratovan Checkpoint (v.2022.12.16.0419, Stratovan). No patch was placed on the trapezium surface because this region was broken in KNM-ER 101000. Landmarks that were homologous and easily locatable (for example, points where three structures met, maxima of curvature) were treated as conventional landmarks and used as anchors to place the patches. The remainder of the landmarks were treated as sliding semi-landmarks. In total, there were 8 landmarks and 235 sliding semi-landmarks. The sliding semi-landmarks were slid along the surfaces in 3D to minimize the bending energy of a thin-plate spline deformation using the function slider3d() in the R package Morpho (v.2.10)<sup>68</sup>. Sliding is an iterative process; specimens were relaxed against the Procrustes mean configuration by sliding along tangent planes until a designated threshold distance (the Procrustes distance between the old and new mean) was reached<sup>68</sup>. After each iteration of the sliding process, the points were projected back onto the surface to avoid the semi-landmarks ‘falling off’ the bone<sup>68–70</sup>. The set of slid landmarks underwent a generalized Procrustes analysis (GPA) and subsequent principal component analysis (PCA) using the function procSym() in the R package Morpho (v.2.10)<sup>68</sup>. The procSym() function returns an array of GPA superimposed coordinates of the translated, scaled and rotated landmark configurations for each specimen. A PCA was then performed on the array of GPA superimposed coordinates, which returned a matrix of principal component (PC) scores. The PC scores were plotted using the function ggplot() in the R package ggplot2 (v.3.4.1)<sup>71</sup>. Point clouds were used to visualize the shape variation along PC axes. Point clouds representing the most negative and positive shapes along the PC axes were generated using plotReftoTarget() in the R package geomorph (v.4.0.4)<sup>72,73</sup>. Comparative sample details are provided in Supplementary Tables 25 and 26.

### Scaphoid and lunate combined shape

A canonical variate analysis of scaphoid and lunate shape (using matched pairs of these carpals) was conducted using angles between articular surfaces and relative surface areas (following the same methods as described above for the trapezoid shape analysis). Comparative sample details are provided in Supplementary Table 27.

### Hamate shape

Variables quantifying functional aspects of hamate form were quantified using landmarks placed on 3D surface scans of KNM-ER 101000 and the comparative sample following previously described methods<sup>74</sup> and summarized in Supplementary Fig. 4c. Details of the comparative sample are provided in Supplementary Tables 28 and 29.

### Radius cross-sectional geometry

The cross-sectional cortical area of the radius of KNM-ER 101000 was measured immediately distal to the radial tuberosity at a level that we estimated to represent 25% of the total physiological length (as defined in a previous study<sup>75</sup>). The comparative dataset for this analysis consisted of radii from a mixed sex sample of recent cadaveric modern humans ( $n = 10$ ) housed in the Department of Anatomical Sciences, Stony Brook University, as well as *P. troglodytes* ( $n = 18$ ) and *Gorilla* spp. ( $n = 24$ ) specimens housed at the American Museum of Natural History (New York City) and the Museum of Comparative Zoology (Harvard University). These comparative specimens were subjected to longitudinal CT scanning using a LightSpeed VCT scanner (GE Healthcare) in the Department of Radiology, Stony Brook University Hospital. The slice thickness was 2.5 mm. Specimens were scanned dry, and a bone-reconstruction algorithm was used. The cross-sectional area of the cortical bone was calculated from DICOM files using the BoneJ plugin<sup>76</sup> for ImageJ software (NIH). Each element was first segmented by the BoneJ automated thresholding protocol 'Optimize Threshold' to extract the bone phase. Structural properties were then analysed on a DICOM slice that was determined to represent 25% of the physiological length using the 'Slice Geometry' function.

### Pedal analyses

The size and composition of the extant sample varied across the analyses of different pedal elements. These are described in Supplementary Tables 38–43. The fossil hominin data were collected from original specimens housed at the following institutions: the Ditsong National Museum of Natural History; the Evolutionary Studies Institute, University of the Witwatersrand; the National Museum of Ethiopia; and the Turkana Basin Institute, Ileret. We supplemented the fossil data using research-quality casts of specimens housed at the following institutions: the National Museum of Kenya (for example, Koobi Fora specimens) and the National Museum of Tanzania (OH 8). We also used published data on base measurements of fossil hominin metatarsal samples<sup>77,78</sup>. For most analyses, we visualized distributions of raw values across species combined with box and whisker plots that display summary statistics such as the median, the interquartile range and the range for each sample.

### Hallucal proximal phalanx

CT data from the New Mexico Decedent Image Database (NMDID) and Primate Research Institute Computed Tomography (PRICT, Kyoto University) were segmented to produce 3D meshes using ORS Dragonfly software. CT data from the Center for Academic Research and Anthropogeny (CARTA, University of California, San Diego) were used to generate 3D meshes using OsiriX software. The remaining individuals were scanned using a NextEngine HD or an Artec Space Spider scanner. We cleaned each 3D model using Geomagic Wrap software (for example, filling small holes and smoothing meshes generated by CT scanning). We calculated the pPP1 dorsal canting angle as the angle between a least-squares plane fit to the proximal articular surface and a plane fit

to the plantar surface defined by three landmarks: the most plantar point on the medial tubercle of the base; the most plantar point on the lateral tubercle of the base; and the most plantar point on the trochlea. We calculated the angle as the inverse cosine of the dot product of the normal vectors of each plane.

### Relative pedal phalangeal lengths

We calculated a phalangeal length ratio (pPP1/pPP5) and a pPP5 length ratio (pPP5 length/pPP5 base mediolateral breadth) from linear measurements collected using Mitutoyo sliding calipers.

### Non-hallucal pedal proximal phalanx articular angle and shaft curvature

The articular angle method was used to quantify the orientation of the metatarsophalangeal joint surface to enable comparisons with previously published data<sup>42</sup>. To quantify the shaft curvature, we used ImageJ software to calculate the included angle from three measurements collected on photographs of pPP5 specimens<sup>79</sup>. The three measurements included the maximum length, the midshaft depth and the projected phalangeal height at the midshaft.

### Pedal proximal phalanx shape

We evaluated the morphometric affinities of the pPP5 of KNM-ER 101000 using PCA. The analysis included nine variables: the included angle of curvature; the dorsal canting ratio; the length; the base mediolateral breadth (BML); the base dorsoplantar depth (BDP); the midshaft mediolateral breadth (MSML); the midshaft dorsoplantar depth (MSDP); the trochlea mediolateral breadth (TML); and the trochlea dorsoplantar depth (TDP). The seven linear distances (length, BML, BDP, MSML, MSDP, TML and TDP) were divided by their geometric mean. The dorsal canting ratio was calculated using two linear measurements: the dorsal interarticular length and the plantar interarticular length. The combination of curvature, ratio and geometric mean-standardized lengths required the use of the correlation matrix in the PCA. We used the 'princomp' function in R (v.4.4.0).

### Metatarsal torsion

We calculated Mt3 torsion using a previously described 3D landmark method<sup>80</sup>. As previously noted, the CT data from NMDID, PRICT and CARTA were segmented to produce 3D meshes using ORS Dragonfly or OsiriX software. All 3D models were imported into Geomagic Wrap for smoothing and/or cleaning before analysis. We digitized six landmarks on each 3D model: the most plantar point of the proximal articular surface at midline (LM1); the most dorsal point of the proximal articular surface at midline (LM2); the centroid of the proximal articular surface (LM3); the most proximal point of the medial tubercle on the plantar Mt head (LM4); the most proximal point of the lateral tubercle on the plantar Mt head (LM5); and the most dorsal point of the Mt head at midline (LM6). A seventh landmark (LM7) was calculated as the midpoint between LM6 and the midpoint of landmarks LM4 and LM5, which positioned it inside the 3D model near the Mt head. The landmarks were used to define a local coordinate reference frame. LM1 and LM2 were used to define a tarsometatarsal joint vector (TMT). LM3 and LM7 were used to define a proximodistal axis vector (PD). LM4 and LM5 were used to define a mediolateral axis vector (ML). The cross-product of PD and ML vectors was used to define a dorsoplantar axis vector (DP). TMT was projected onto the same plane as DP, and the metatarsal torsion angle was calculated as the rotation of TMT relative to DP using the atan2 function. The resulting angular rotation value was converted from radians to degrees (where 1 radian = 180°/π). For right metatarsals viewed from their proximal ends, a positive torsion value indicates a counterclockwise rotation, whereas a negative torsion angle indicates a clockwise rotation of DP relative to TMT for comparability with previous studies<sup>80–83</sup>. Metatarsal torsion angles were calculated using a custom Matlab script.

## Metatarsal base ratio

We computed the ratio of Mt3 base dorsoplantar to mediolateral dimensions using linear distances (Mt3 BDP/BML).

## Ancestral state reconstruction methods

To reconstruct patterns of hand evolution across the hominin phylogeny, we constructed a character matrix consisting of 20 discrete morphological characteristics across the manus (Supplementary Table 44). The previously proposed characteristics<sup>3</sup> served as the starting point for this matrix (Supplementary Table 45). We then coded character states for 6 extant species and 14 fossil taxa when preserved elements permitted the assessment of a given character. In most cases, we based these character codings on fossils that were unequivocally attributed to a taxon (for example, category A in ref. 13). The following samples were exceptions to this criterion: OH 7, which we coded as *H. habilis*; SK 84 was taken to represent *P. robustus*; and all Sterkfontein Member 4 fossils were considered to represent *A. africanus*. KNM-ER 101000 was treated as the sole representative of *P. boisei*, although it never substantially differed from the character states observed in KNM-ER 47000. The tree topology used for ancestral state reconstructions was based on the most parsimonious tree recovered per a previous study<sup>22</sup>. Ancestral state reconstructions were conducted individually for each character along the tree using maximum parsimony in Mesquite (v. 3.61)<sup>84</sup>. No character ordering or polarity was assumed a priori.

## Reporting summary

Further information on research design is available in the Nature Portfolio Reporting Summary linked to this article.

## Data availability

3D surface scans of the KNM-ER 101000 fossils are available to view, manipulate and measure at MorphoSource (<https://www.morpho-source.org>). A full list of digital object identifiers is provided in Supplementary Table 46. All 2D measurements recorded by the authors are also provided in the Supplementary Information.

## Code availability

The custom metatarsal torsion Matlab script is available at Figshare (<https://doi.org/10.6084/m9.figshare.29991643>)<sup>85</sup>.

61. du Plessis, A., le Roux, S. G. & Guelpa, A. The CT scanner facility at Stellenbosch University: an open access X-ray computed tomography laboratory. *Nucl. Instrum. Methods Phys. Res. B* **384**, 42–49 (2016).
62. Robinson, J. T. *Dentition of the Australopithecinae* Vol. Memoir No. 9 (Transvaal Museum, 1956).
63. Grine, F. E., Martin, L. B. in *Evolutionary History of the 'Robust' Australopithecines* (ed. Grine, F. E.) 3–42 (Aldine de Gruyter, 1988).
64. Stern, J. T. Jr, Jungers, W. L. & Susman, R. L. Quantifying phalangeal curvature: an empirical comparison of alternative methods. *Am. J. Phys. Anthropol.* **97**, 1–10 (1995).
65. Domínguez-Rodrigo, M. et al. Earliest modern human-like hand bone from a new >1.84-million-year-old site at Olduvai in Tanzania. *Nat. Commun.* **6**, 7987 (2015).

66. Tocheri, M. W. et al. Functional capabilities of modern and fossil hominid hands: three-dimensional analysis of trapezia. *Am. J. Phys. Anthropol.* **122**, 101–112 (2003).
67. Tocheri, M. W., Razdan, A., Williams, R. C. & Marzke, M. W. A 3D quantitative comparison of trapezium and trapezoid relative articular and nonarticular surface areas in modern humans and great apes. *J. Hum. Evol.* **49**, 570–586 (2005).
68. Schlager, S. in *Statistical Shape and Deformation Analysis* 217–256 (Elsevier, 2017).
69. Gunz, P., Mitteroecker, P. & Bookstein, F. L. in *Developments in Primatology: Progress and Prospects* (eds Zheng, G. et al.) 73–98 (Kluwer Academic–Plenum, 2006).
70. Gunz, P. & Mitteroecker, P. Semilandmarks: a method for quantifying curves and surfaces. *Hystrix* **24**, 103–109 (2013).
71. Wickham, H. *Ggplot2* (Springer International, 2016).
72. Adams, D. C. & Otárola-Castillo, E. geomorph: an rpackage for the collection and analysis of geometric morphometric shape data. *Methods Ecol. Evol.* **4**, 393–399 (2013).
73. Baken, E. K., Collyer, M. L., Kaliontzopoulou, A. & Adams, D. C. geomorph v4.0 and gmShiny: enhanced analytics and a new graphical interface for a comprehensive morphometric experience. *Methods Ecol. Evol.* **12**, 2355–2363 (2021).
74. Orr, C. M. et al. New wrist bones of *Homo floresiensis* from Liang Bua (Flores, Indonesia). *J. Hum. Evol.* **64**, 109–129 (2013).
75. Mongle, C. S., Wallace, I. J. & Grine, F. E. Cross-sectional structural variation relative to midshaft along hominine diaphyses. I. The forelimb. *Am. J. Phys. Anthropol.* **158**, 386–397 (2015).
76. Doube, M. BoneJ: free and extensible bone image analysis in ImageJ. *Bone* **47**, 1076–1079 (2010).
77. Harcourt-Smith, W. E. H. et al. The foot of *Homo naledi*. *Nat. Commun.* **6**, 8432 (2015).
78. Desilva, J. M., McNutt, E., Zipfel, B., Ward, C. V. & Kimbel, W. H. Associated *Australopithecus afarensis* second and third metatarsals (A.L. 333-133) from Hadar, Ethiopia. *J. Hum. Evol.* **146**, 102848 (2020).
79. Susman, R. L., Stern, J. T. & Jungers, W. L. Arboreality and bipedality in the Hadar hominids. *Folia Primatol.* **43**, 113–156 (1984).
80. Goodenberger, K. E. et al. Functional morphology of the hallucal metatarsal with implications for inferring grasping ability in extinct primates. *Am. J. Phys. Anthropol.* **156**, 327–348 (2015).
81. Pontzer, H. et al. Locomotor anatomy and biomechanics of the Dmanisi hominins. *J. Hum. Evol.* **58**, 492–504 (2010).
82. DeSilva, J. M., Proctor, D. J. & Zipfel, B. A complete second metatarsal (StW 89) from Sterkfontein Member 4, South Africa. *J. Hum. Evol.* **63**, 487–496 (2012).
83. Drapeau, M. S. M. & Harmon, E. H. Metatarsal torsion in monkeys, apes, humans and australopithecines. *J. Hum. Evol.* **64**, 93–108 (2013).
84. Maddison, W. P. & Maddison, D. R. Mesquite: a modular system for evolutionary analysis. *Mesquite* <https://www.mesquiteproject.org> (2003).
85. Prang, T. C. Custom MATLAB script for metatarsal torsion calculation. *Figshare* <https://doi.org/10.6084/m9.figshare.29991643> (2025).

**Acknowledgements** This study was funded by multiple grants from the Turkana Basin Research Fund and the National Geographic Society. C.S.M. thanks the Stony Brook Research Foundation for funding. We thank the National Museums of Kenya, NACOSTI and the Turkana Basin Institute for facilitation of this work; T. Gichunge for surface scanning of the fossil specimens; N. Robert for photography; F. Spoor for providing comments on an earlier draft and for sharing measurements of the M3 specimens from OH 62 and KNM-ER 17400; and R. Leakey for his enthusiasm and support that made these discoveries possible. F. Tre Lawrence illustrated the hand outline used in Fig. 3. This Article was improved by feedback from T. Kivell and B. Wood.

**Author contributions** C.S.M., L.N.L., C.M.O. and M.W.T. conceived and designed the study. C.S.M., T.C.P., F.E.G., C.M.O., M.W.T., B.A.P., O.L., T.E.H., S.M., J.R. and W.M. collected the data and conducted analyses. L.N.L., M.G.L., J.L., W.W.H., H.S., A.U., P.Y., I.D., M.K., E. Linga, R.L., A.L., M.L., E. Lonyericho, I.L., N.N. and C.N. conducted field identification and excavation of fossil specimens. A.D.P. contributed analysis tools. C.F. established the stratigraphical context. C.S.M., C.M.O., M.W.T. and T.C.P. wrote the manuscript with input from all authors.

**Competing interests** The authors declare no competing interests.

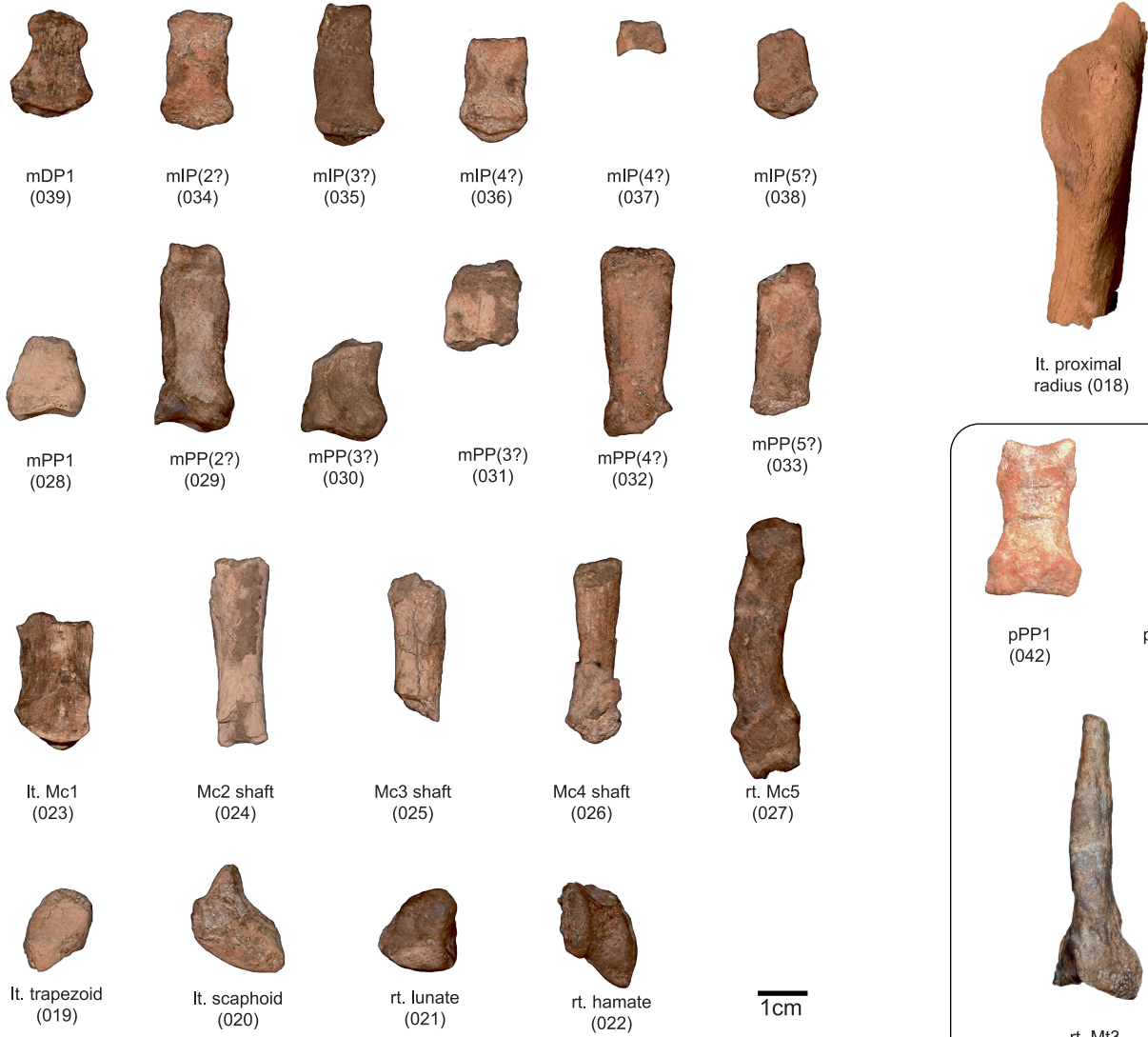
## Additional information

**Supplementary information** The online version contains supplementary material available at <https://doi.org/10.1038/s41586-025-09594-8>.

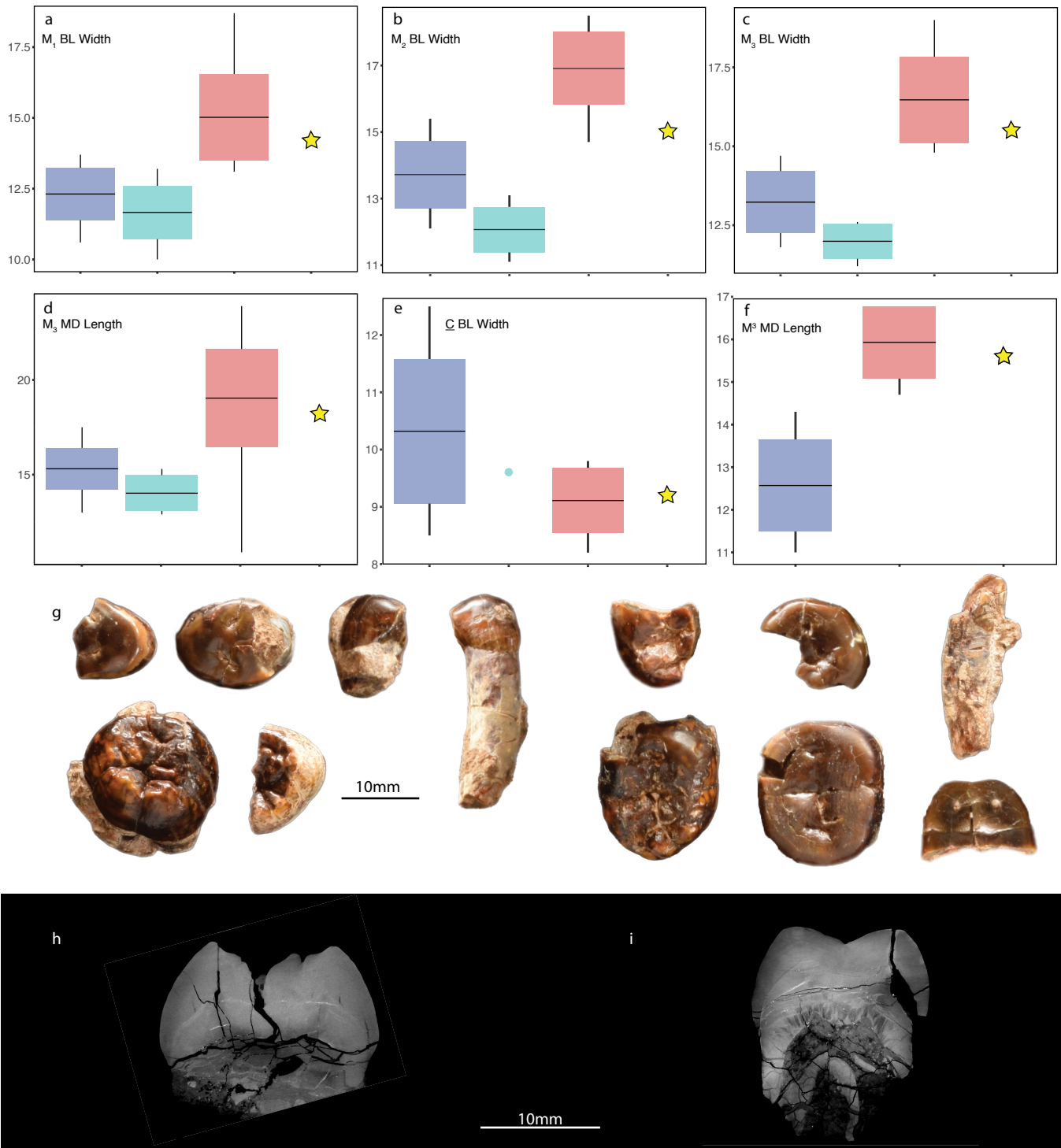
**Correspondence and requests for materials** should be addressed to Carrie S. Mongle.

**Peer review information** Nature thanks Tracy Kivell, Bernard Wood and the other, anonymous, reviewer(s) for their contribution to the peer review of this work.

**Reprints and permissions information** is available at <http://www.nature.com/reprints>.

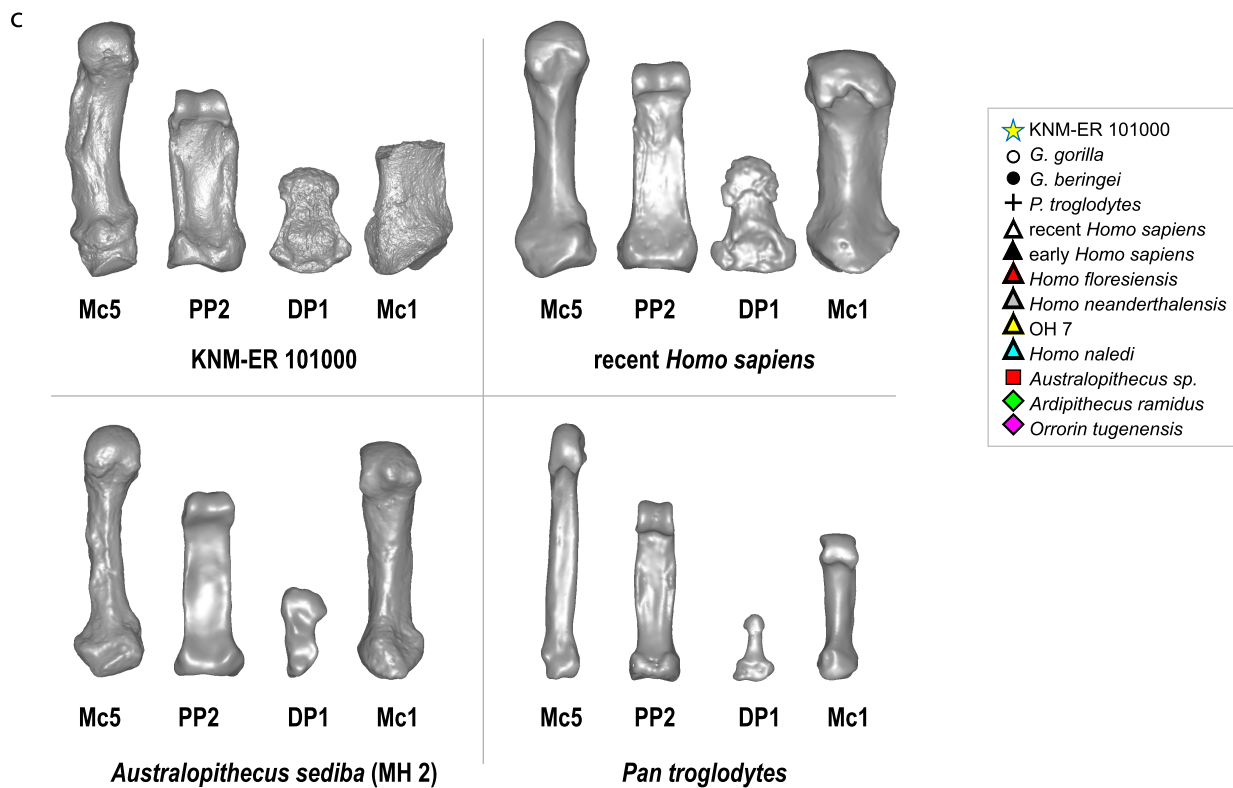
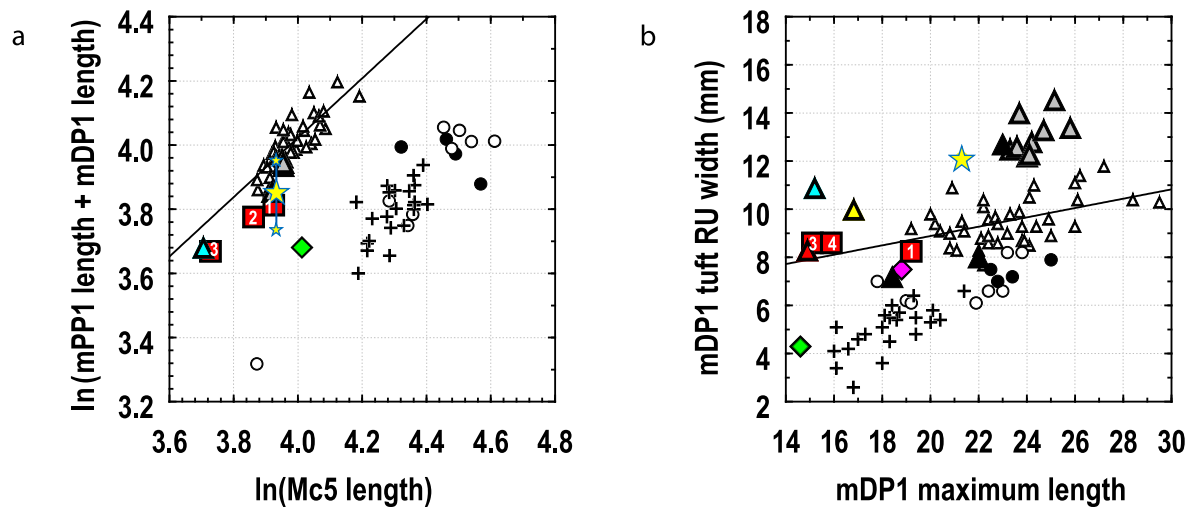


**Extended Data Fig. 1 | Postcranial remains of KNM-ER101000.** Manual elements shown in palmar view. Proximal radius positioned to show radial tuberosity. Box contains pedal elements shown in dorsal view.



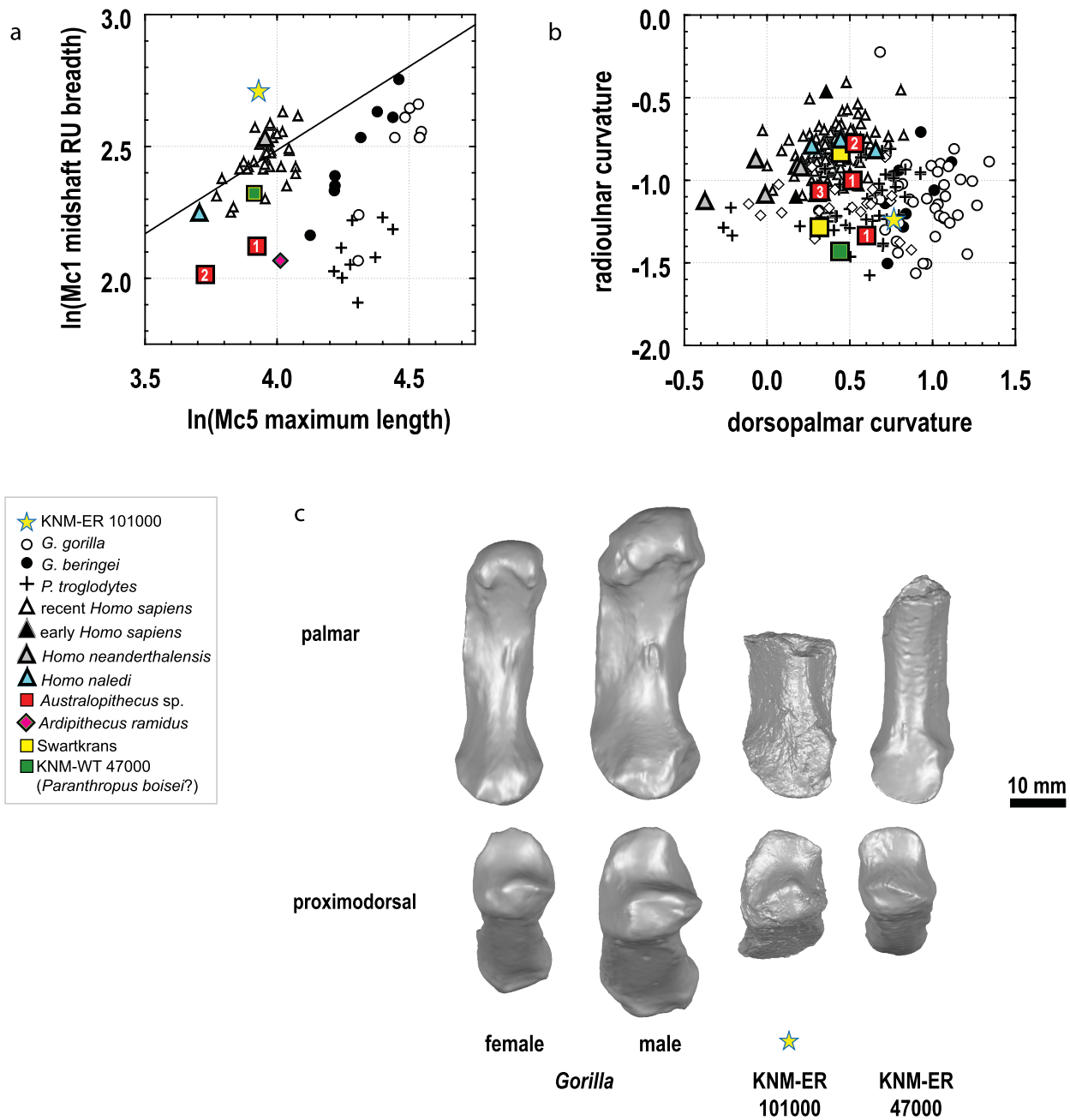
**Extended Data Fig. 2 | a-f) KNM-ER101000 dentition and comparative dental metrics.** Boxplots depicting linear dental metrics in early *Homo* (purple), *Homo erectus* (light blue), and *Paranthropus boisei* (red). KNM-ER101000 is shown as a yellow star in each panel. Data are shown as boxplots, with the median indicated by a horizontal line, the box spanning the interquartile range (IQR), and the whiskers extending to  $1.5 \times$  IQR from each quartile. Individual fossil

specimens included in each plot are listed in Supplementary Tables 6–10. **g)** Photographs show the KNM-ER101000 maxillary and mandibular dentition. The postcanine dentition is shown in occlusal or near occlusal ( $RM^3$ ) view, while the canines are in labial view. CT sections taken perpendicular to the mesiodistal axis through the apices of the dentine horns of the mesial cusps of the maxillary  $RM^3$  (**h**) and the mandibular  $RM_3$  (**i**).



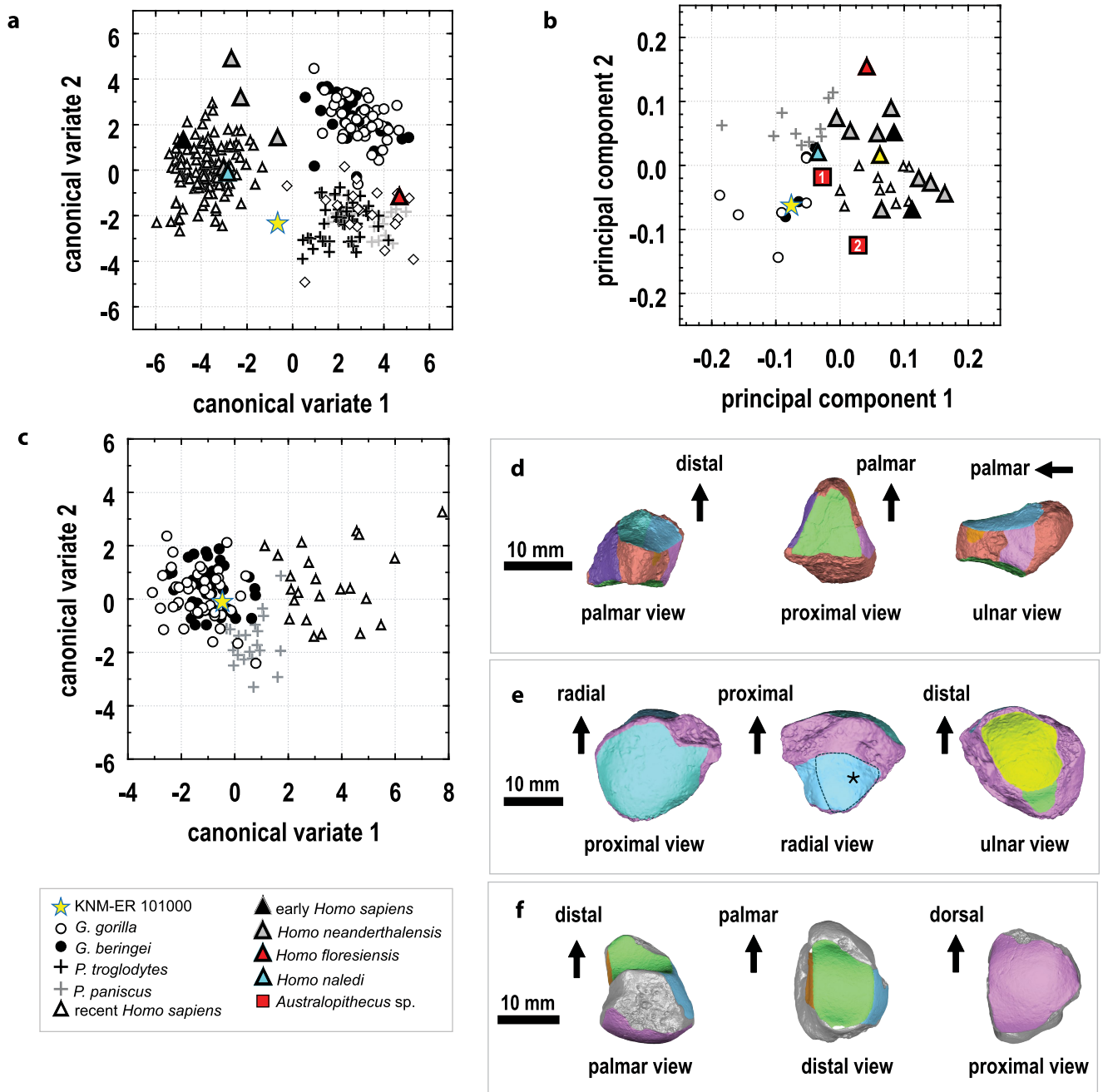
**Extended Data Fig. 3 | Digital proportions in KNM-ER101000.** a) natural log plot of the combined estimated length of the proximal pollical phalanx (mPP1) and distal pollical phalanx (mDP1) versus fifth metacarpal (Mc5 maximum length) with a least-squares regression line through the recent *H. sapiens* sample [ $\ln(\text{mPP1\_length} + \text{mDP1\_length}) = 0.93 * \ln(\text{Mc5\_maximum\_length}) - 0.32$ ;  $p < 0.001$ ,  $r^2 = 0.69$ ]; b) plot of mDP1 tuft RU breadth versus mDP1 maximum length a least-squares regression line through the recent *H. sapiens* sample [ $\text{mDP1\_tuft\_RU\_width} = 0.19 * \text{mDP1\_maximum\_length} + 5.0$ ;  $p < 0.01$ ,

$r^2 = 0.23$ ]; c) 3D surface model renderings of the KNM-ER101000 digital specimens shown with relevant comparative specimens, which are all visually scaled to the same Mc5 maximum length as KNM-ER 101000. The central star in (a) includes the mean estimate for the mPP1 length and the upper and lower stars represent the 95% confidence interval of that estimate. *Australopithecus* sample: 1 = *A. afarensis* [plot in (a) includes AL 333-69 mPP1 + AL 333-159 mDP1 and mean of AL 333-14, AL 333-89, and AL 333-141 Mc5s and plot in (b) includes AL 333-159]. 2 = “*A. prometheus*” StW 573. 3 = *A. sediba* MH2. 4 = *A. africanus* StW 294.



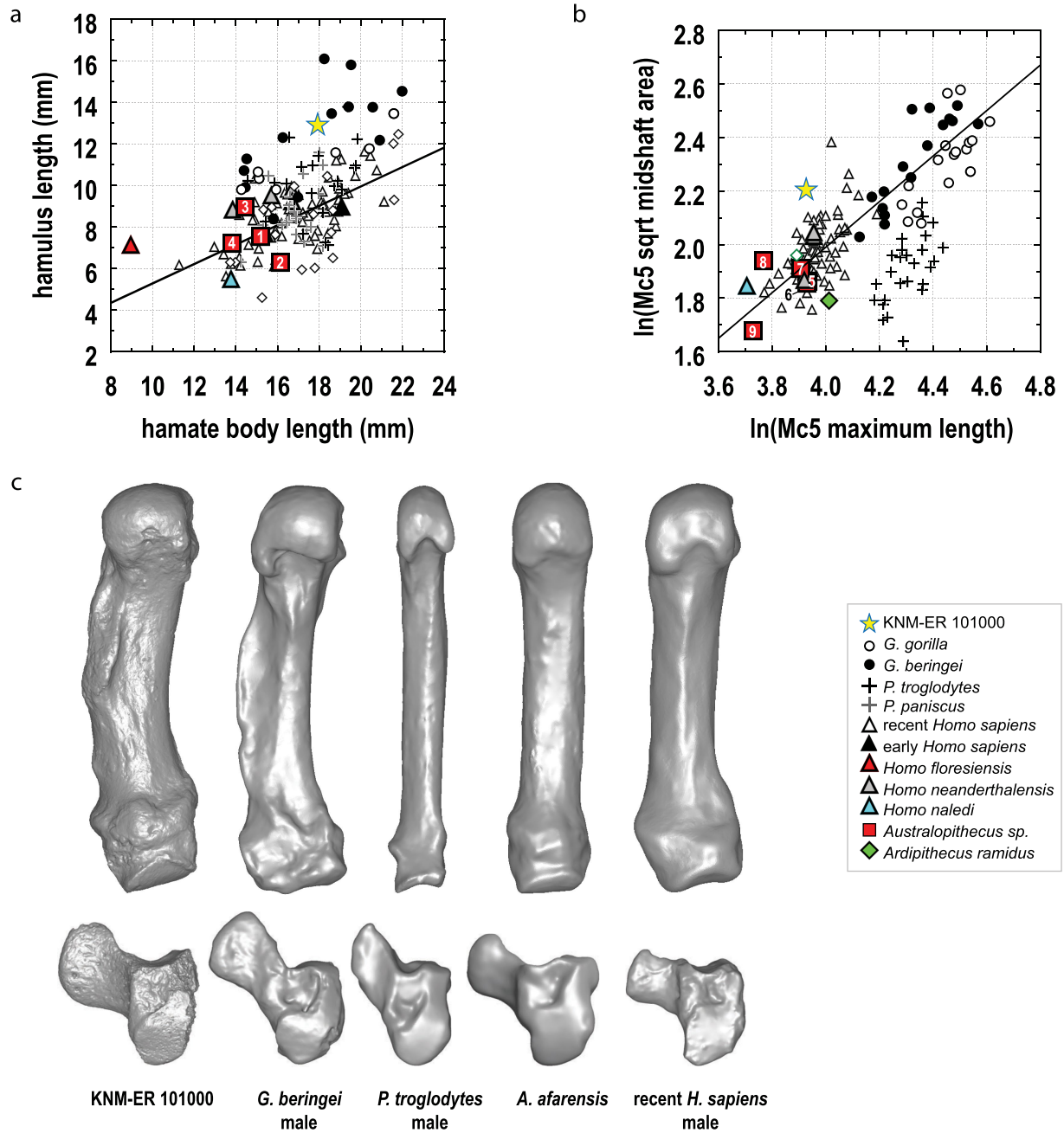
**Extended Data Fig. 4 | Morphology of the first metacarpal in KNM-ER 101000.** A robust first metacarpal (Mc1) shaft in KNM-ER 101000 is combined with a presumably primitive (African-ape-like) morphology of the first carpometacarpal joint. **a)** natural log plot of the Mc1 radioulnar (RU) midshaft width versus maximum length of the fifth metacarpal (Mc5) with least-squares regression line through the recent *H. sapiens* sample [ $\ln\text{MC1\_midshaft\_RU} = 0.63 * \ln(\text{Mc5\_max\_length}) - 0.05$ ; ( $p < 0.001, r^2 = 0.28$ )]; **b)** bivariate plot of the

curvatures of the Mc1's proximal articular surface (for the trapezium); **c)** renderings of Mc1s from a female gorilla, a male gorilla, KNM-ER 101000, and KNM-ER 47000. *Australopithecus* sample: 1 = *A. afarensis* (AL 333w-39 and -58 Mc1s each plotted against the mean of the Mc5 specimens—they overlap in the plot because the two Mc1s differ by only 0.6 mm in midshaft RU breadth); 2 = *A. sediba* MH2; 3 = *A. africanus* StW 418.



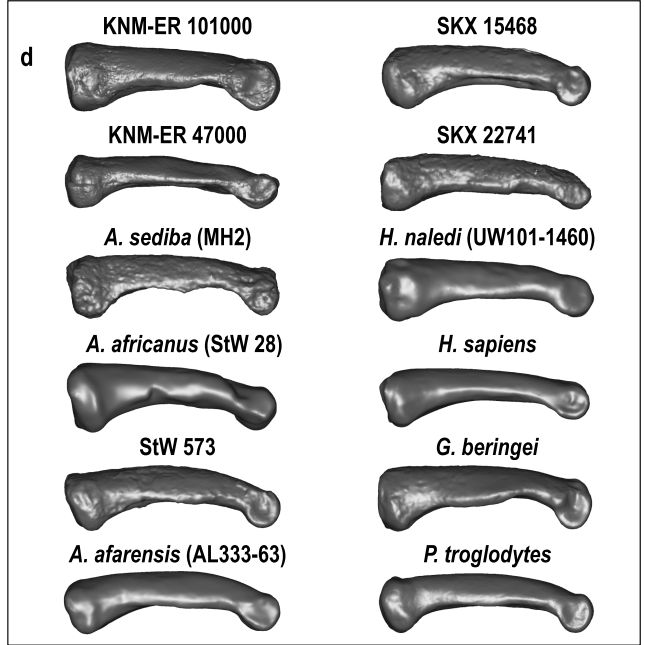
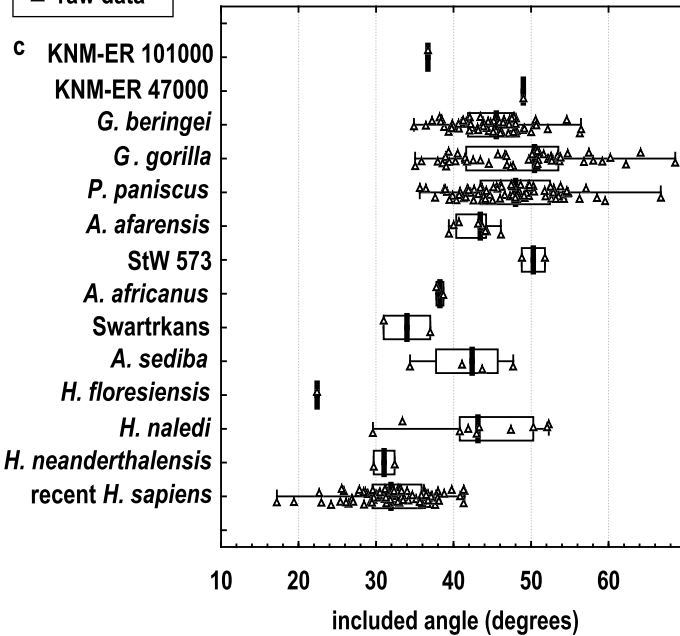
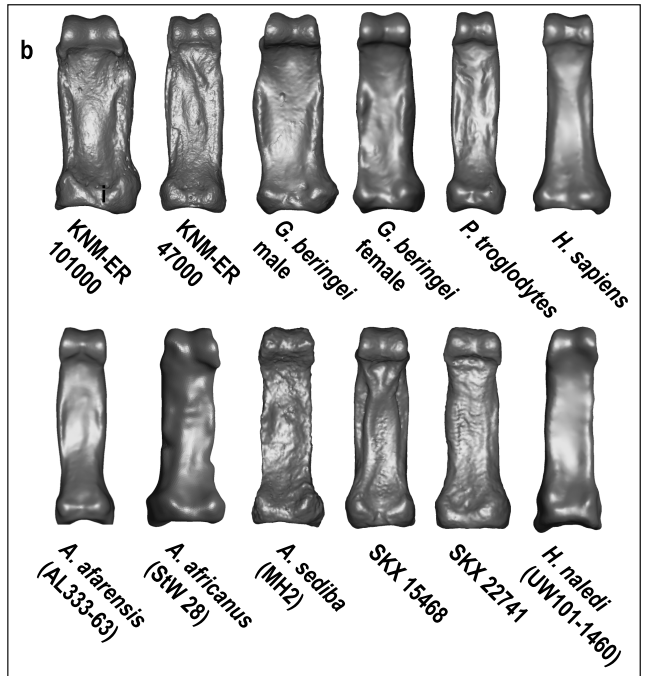
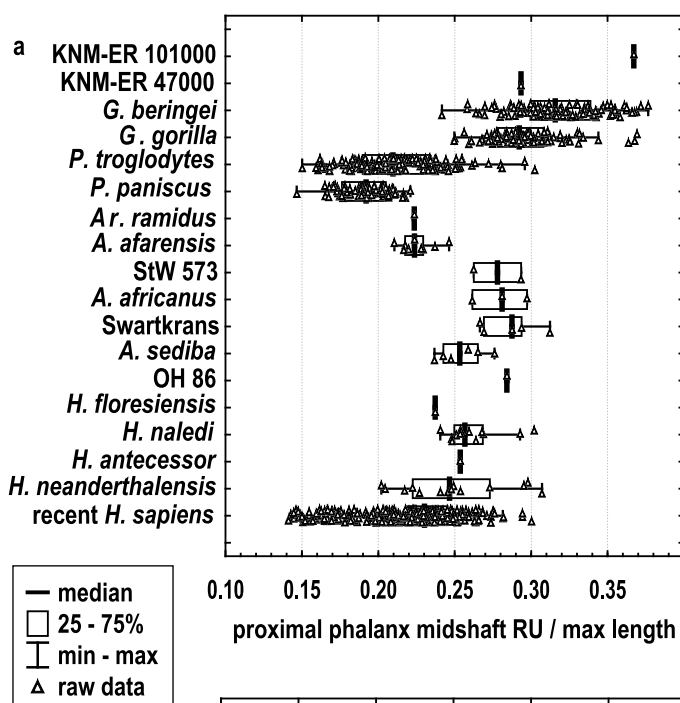
**Extended Data Fig. 5 | Morphology of the trapezoid, scaphoid, and lunate in KNM-ER 101000.** **a)** canonical variates plot including joint angles and surface areas of the trapezoid; **b)** principal components plot showing results of a 3D geometric morphometrics analysis of scaphoid shape; **c)** canonical variates plot including joint angles and surface areas for the scaphoid and lunate combined; **d)** rendering of the KNM-ER 101000 trapezoid; **e)** renderings of the

of the KNM-ER 101000 scaphoid (dotted outline indicates the articular area for the trapezoid and the asterisk indicates the portion that is typically reduced in *H. sapiens* in response to the shape changes of the trapezoid and capitate, resulting in a scaphocapitate joint that is open distally); **f)** renderings of the KNM-ER 101000 lunate. *Australopithecus* sample: 1 = *Australopithecus* sp. StW 618; 2 = *A. sediba* MH2.



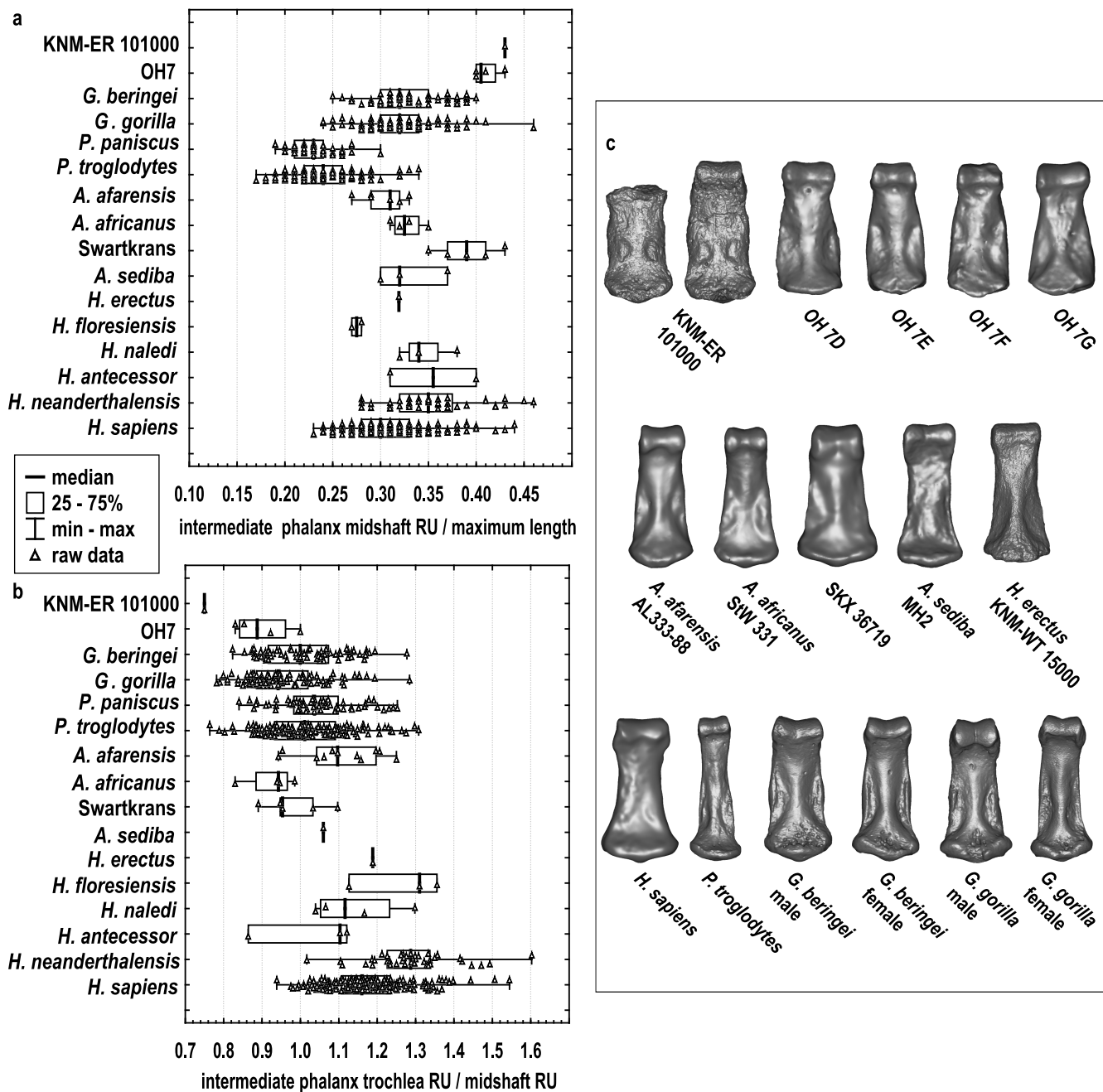
**Extended Data Fig. 6 | Hypothenar morphology in KNM-ER101000.** Well-developed hypothenar morphology (hamate hamulus and Mc5) of the KNM-ER101000 specimen (yellow star throughout). **a**) Hamulus length versus hamate body length; **b**) natural log-log plot of the square root (sqrt) of the area (radioulnar width x dorsopalmar depth) of the Mc5 at midshaft versus the Mc5 maximum length **c**) 3D surface model renderings of the KNM-ER101000 hamate and Mc5 and comparative specimens. Mc5s are scaled to the same proximodistal length and hamates are scaled to the same proximodistal body length. The least squares regression lines are fit to the *Homo sapiens* samples (excluding

one individual with pituitary dwarfism and one with gigantism in the hamate analysis);  $\text{hamulus\_length} = 0.62 + 0.47 * \text{hamate\_body\_length}$  ( $p < 0.001, r^2 = 0.44$ );  $\ln(\text{Mc5\_sqrt\_midshaft\_area}) = -1.41 + 0.85 * \ln(\text{Mc5\_maximum\_length})$  ( $p < 0.001, r^2 = 0.33$ ). *Australopithecus* sample: 1 = *A. afarensis* AL 333-50 hamate, 2 = *A. cf. afarensis* KNM-WT 22994-H hamate, 3 = *A. sediba* MH2 left hamate, 4 = *A. sediba* MH2 right hamate). Fossil hominins in the Mc5 plot (E): taxa symbols follow the hamate plots with addition of *Ar. ramidus* (green diamond) and for the *Australopithecus* spp. specimens 5 = *A. afarensis* AL 333-14, 6 = *A. afarensis* AL 333-89, 7 = *A. afarensis* AL 333-141, 8 = *A. sediba* MH2, 9 = *A. africanus* StW 63.



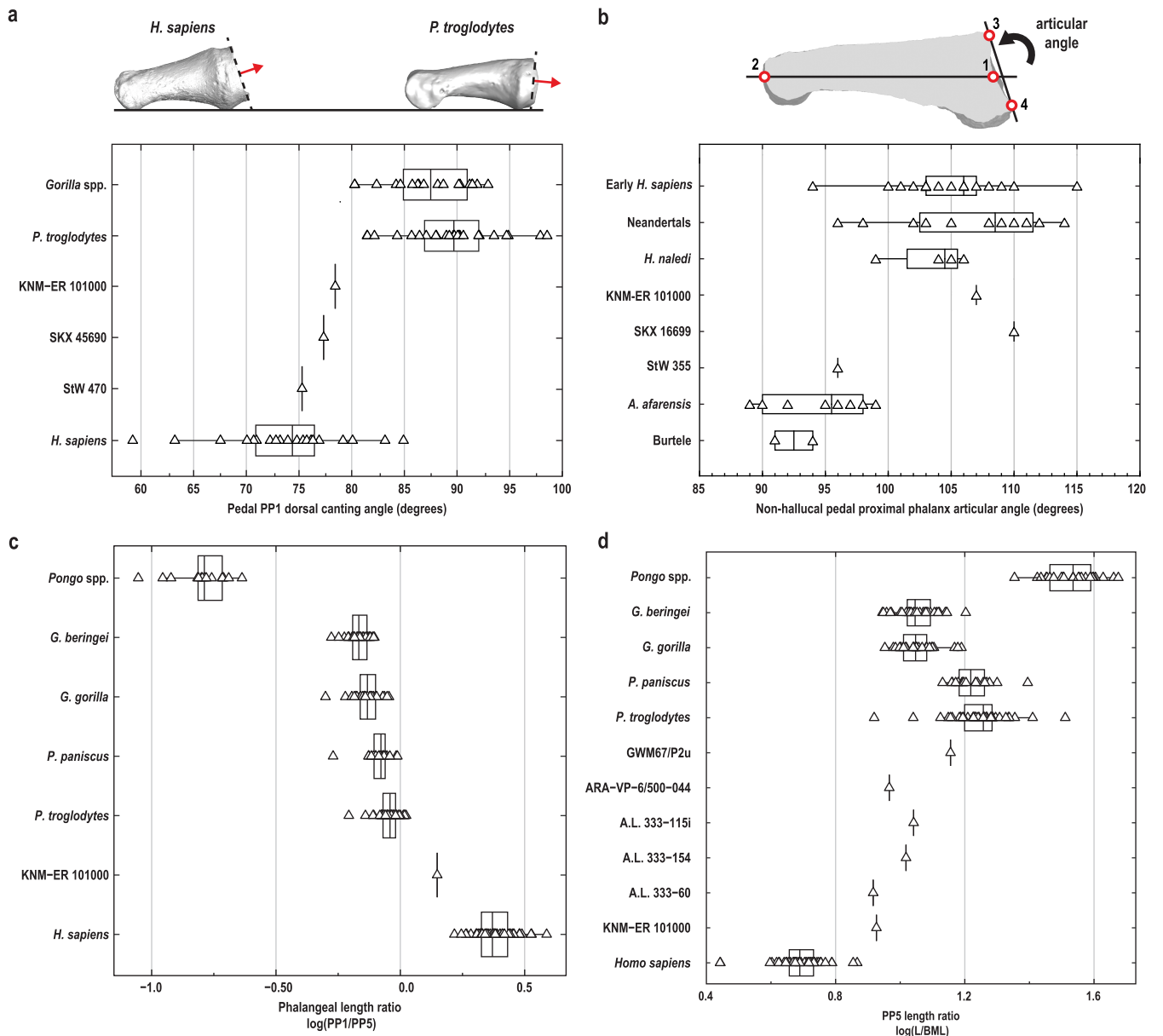
**Extended Data Fig. 7 | Manual proximal phalanx morphology in KNM-ER 101000.** Manual proximal phalanges robusticity (a,b) and longitudinal shaft curvature (c,d). RU = radioulnar width. Data presented in a) consist of the following samples: KNM-ER 101000 n = 1, KNM-ER 47000 n = 1, *G. beringei* n = 109, *G. gorilla* n = 96, *P. troglodytes* n = 152, *P. paniscus* n = 66, *Ar. ramidus* n = 1, *A. afarensis* n = 8, StW 573 n = 2, *A. africanus* n = 3, Swartkrans n = 5, *A. sediba* n = 4, OH 86 n = 1, *H. floresiensis* n = 1, *H. naledi* n = 11, *H. antecessor* n = 1, *H. neanderthalensis* n = 13, recent *H. sapiens* n = 216. Data presented in c)

consist of the following samples: KNM-ER 101000 n = 1, KNM-ER 47000 n = 1, *G. beringei* n = 68, *G. gorilla* n = 96, *P. troglodytes* n = 68, *P. paniscus* n = 84, *A. afarensis* n = 7, StW 573 n = 2, *A. africanus* n = 3, Swartkrans n = 2, *A. sediba* n = 4, OH 86 n = 1, *H. floresiensis* n = 1, *H. naledi* n = 8, *H. antecessor* n = 1, *H. neanderthalensis* n = 2, recent *H. sapiens* n = 96. In both boxplots (a,c) the median is indicated by a horizontal line, the box spans the interquartile range (IQR), and the whiskers represent the minimum and maximum values in the sample.



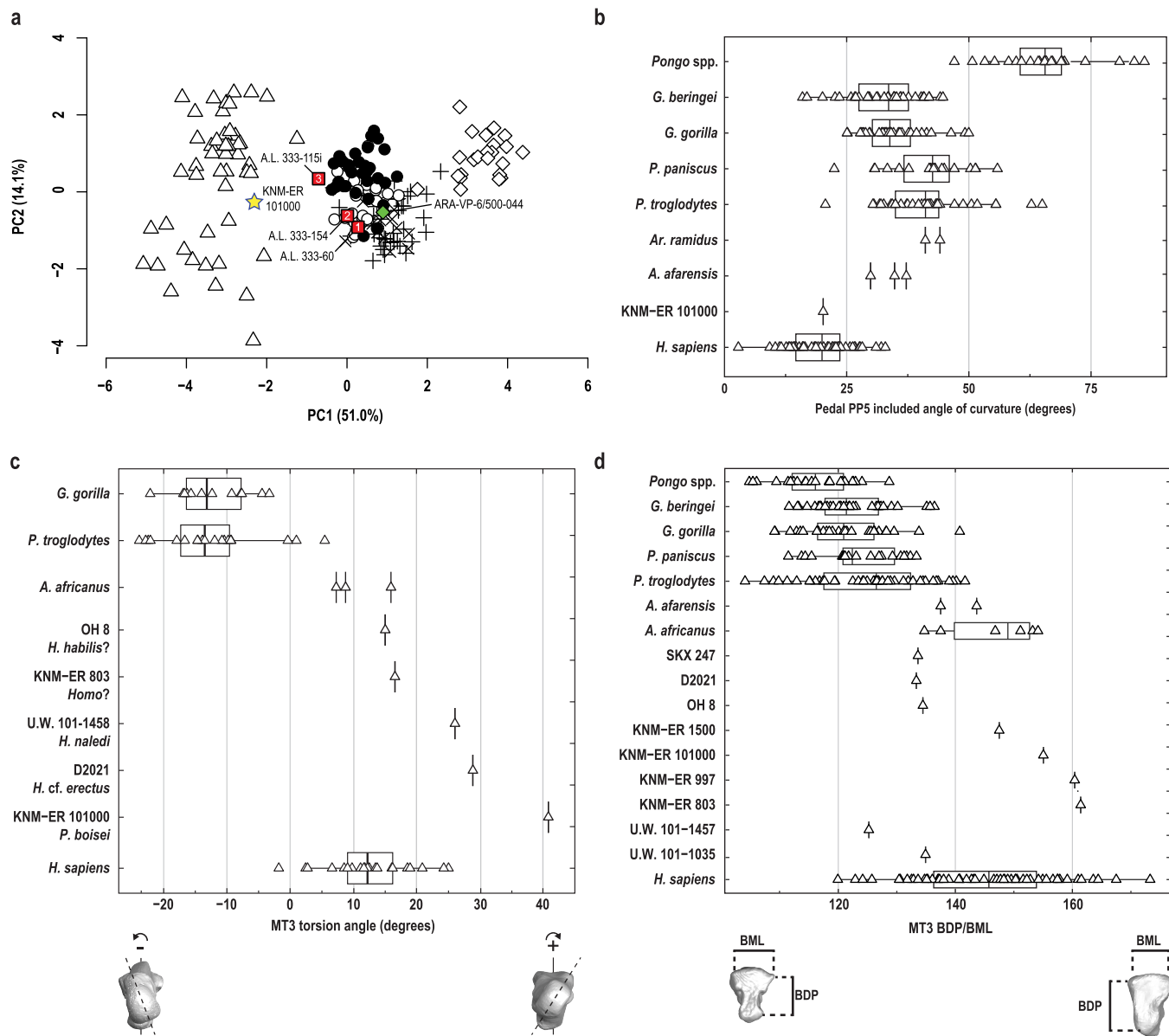
**Extended Data Fig. 8 | Manual intermediate phalanx robusticity in KNM-ER 101000.** RU = radioulnar width. OH 7 and KNM-WT 15000 are juveniles and are missing the proximal epiphyses. Raw lengths (without epiphyses) are used in the calculation of the index plotted in (a). Data on primate epiphyseal thicknesses are scant. Conservative upper estimates of the added length added by epiphyses (an additional 2.0 mm) would put the median index slightly lower for the OH 7 specimens at 0.38 (maximum 0.39, minimum 0.37) and thus closer to the Swartkrans sample. Similarly, when the KNM-WT 15000 phalanx is estimated at an additional 2.0 mm length with epiphysis, it results in an index of 0.29. However, the growth allometry of length and width for early hominin intermediate phalanges is unknown, so caution is warranted in interpreting these metrics for such juvenile individuals. Data presented in a) consist of the following samples:

KNM-ER101000 n = 1, OH7 n = 4, *G. beringei* n = 77, *G. gorilla* n = 48, *P. troglodytes* n = 68, *P. paniscus* n = 59, *A. afarensis* n = 11, *A. africanus* n = 4, Swartkrans n = 5, *A. sediba* n = 3, *H. erectus* n = 1, *H. floresiensis* n = 2, *H. naledi* n = 4, *H. neanderthalensis* n = 42, recent *H. sapiens* n = 155. Data presented in b) consist of the following samples: KNM-ER101000 n = 1, OH7 n = 4, *G. beringei* n = 77, *G. gorilla* n = 48, *P. troglodytes* n = 68, *P. paniscus* n = 59, *A. afarensis* n = 11, *A. africanus* n = 4, Swartkrans n = 5, *A. sediba* n = 1, *H. erectus* n = 1, *H. floresiensis* n = 3, *H. naledi* n = 4, *H. neanderthalensis* n = 42, recent *H. sapiens* n = 155. In both boxplots (a,b) the median is indicated by a horizontal line, the box spans the interquartile range (IQR), and the whiskers represent the minimum and maximum values in the sample. c) illustrates the observed morphology in a sample of hominin and extant ape intermediate phalanges.



**Extended Data Fig. 9 | Pedal proximal phalanx morphology in KNM-ER 101000.** Relative length and proximal articular surface morphology of the KNM-ER 101000 pedal proximal phalanges. **(a)** Dorsal canting angle of the hallux proximal phalanx. **(b)** Proximal articular angle of the non-halluxal pedal proximal phalanx. **(c)** PP1 to PP5 length ratio. **(d)** PP5 length to base mediolateral breadth ratio. Note that KNM-ER 101000 has a non-halluxal

proximal phalanx articular angle within the range of the fossil *Homo* sample combined with intrinsic length reduction compared to *Ar. ramidus* and *A. afarensis*. In each boxplot (a-d) the median is indicated by a horizontal line, the box spans the interquartile range (IQR), and the whiskers represent the minimum and maximum values in the sample.



**Extended Data Fig. 10 | Pedal proximal phalanx shape and metatarsal torsion in KNM-ER101000.** Analyses of pedal proximal phalanx shape, included angle of proximal phalanx curvature, and third metatarsal variables. **(a)** PCA on 9 variables reflecting the intrinsic dimensions, curvature, and base dorsal canting ratio of the pPP5. Individuals on the positive end of PC1 have increased curvature, decreased dorsal canting, increased intrinsic length, and a mediolaterally narrower base and trochlea. Individuals on the positive end of PC2 have mediolaterally wider and dorsoplantarly shallower midshafts. Open triangles = *H. sapiens*, black crosses = *P. troglodytes*, grey crosses = *P. paniscus*, open black circle = *G. gorilla*, solid black circle = *G. beringei*, open black diamonds = *Pongo*

spp., green diamond = *Ar. ramidus* (ARA-VP-6/500-044), red squares = *A. afarensis* (1 = A.L. 333-115i, 2 = A.L. 333-154, 3 = A.L. 333-60), gold star = KNM-ER 101000. **(b)** Pedal PP5 included angle of curvature. **(c)** MT3 torsion angle. **(d)** Third metatarsal base dorsoplantar height to mediolateral breadth ratio. KNM-ER 101000 has a more derived, *Homo*-like pPP5 combined with high metatarsal torsion and a dorsoplantarly deep tarsometatarsal joint. In each boxplot (b-d) the median is indicated by a horizontal line, the box spans the interquartile range (IQR), and the whiskers represent the minimum and maximum values in the sample.

## Reporting Summary

Nature Portfolio wishes to improve the reproducibility of the work that we publish. This form provides structure for consistency and transparency in reporting. For further information on Nature Portfolio policies, see our [Editorial Policies](#) and the [Editorial Policy Checklist](#).

### Statistics

For all statistical analyses, confirm that the following items are present in the figure legend, table legend, main text, or Methods section.

n/a Confirmed

- The exact sample size ( $n$ ) for each experimental group/condition, given as a discrete number and unit of measurement
- A statement on whether measurements were taken from distinct samples or whether the same sample was measured repeatedly
- The statistical test(s) used AND whether they are one- or two-sided  
*Only common tests should be described solely by name; describe more complex techniques in the Methods section.*
- A description of all covariates tested
- A description of any assumptions or corrections, such as tests of normality and adjustment for multiple comparisons
- A full description of the statistical parameters including central tendency (e.g. means) or other basic estimates (e.g. regression coefficient) AND variation (e.g. standard deviation) or associated estimates of uncertainty (e.g. confidence intervals)
- For null hypothesis testing, the test statistic (e.g.  $F$ ,  $t$ ,  $r$ ) with confidence intervals, effect sizes, degrees of freedom and  $P$  value noted  
*Give  $P$  values as exact values whenever suitable.*
- For Bayesian analysis, information on the choice of priors and Markov chain Monte Carlo settings
- For hierarchical and complex designs, identification of the appropriate level for tests and full reporting of outcomes
- Estimates of effect sizes (e.g. Cohen's  $d$ , Pearson's  $r$ ), indicating how they were calculated

*Our web collection on [statistics for biologists](#) contains articles on many of the points above.*

### Software and code

Policy information about [availability of computer code](#)

Data collection

NA

Data analysis

Custom metatarsal torsion Matlab script available at <https://doi.org/10.6084/m9.figshare.29991643>

For manuscripts utilizing custom algorithms or software that are central to the research but not yet described in published literature, software must be made available to editors and reviewers. We strongly encourage code deposition in a community repository (e.g. GitHub). See the Nature Portfolio [guidelines for submitting code & software](#) for further information.

### Data

Policy information about [availability of data](#)

All manuscripts must include a [data availability statement](#). This statement should provide the following information, where applicable:

- Accession codes, unique identifiers, or web links for publicly available datasets
- A description of any restrictions on data availability
- For clinical datasets or third party data, please ensure that the statement adheres to our [policy](#)

Three-dimensional surface scans of the KNM-ER 101000 fossils are available at (morposouce DOI). All 2D measurements of KNM-ER 101000 are provided in the supplementary information.

## Research involving human participants, their data, or biological material

Policy information about studies with [human participants or human data](#). See also policy information about [sex, gender \(identity/presentation\), and sexual orientation](#) and [race, ethnicity and racism](#).

Reporting on sex and gender	NA
Reporting on race, ethnicity, or other socially relevant groupings	NA
Population characteristics	NA
Recruitment	NA
Ethics oversight	NA

Note that full information on the approval of the study protocol must also be provided in the manuscript.

## Field-specific reporting

Please select the one below that is the best fit for your research. If you are not sure, read the appropriate sections before making your selection.

Life sciences     Behavioural & social sciences     Ecological, evolutionary & environmental sciences

For a reference copy of the document with all sections, see [nature.com/documents/nr-reporting-summary-flat.pdf](https://www.nature.com/documents/nr-reporting-summary-flat.pdf)

## Ecological, evolutionary & environmental sciences study design

All studies must disclose on these points even when the disclosure is negative.

Study description	Description of new hominin fossil (KNM-ER 101000)
Research sample	Comparative sample of hominin fossils, modern Homo sapiens, and African apes
Sampling strategy	Available and complete museum specimens
Data collection	Data were collected using 2D measurements of original specimens, published metrics, and 3D surface scans
Timing and spatial scale	Spatial scale of excavation reported in map grid (Figure 1)
Data exclusions	NA
Reproducibility	NA
Randomization	NA
Blinding	NA

Did the study involve field work?  Yes     No

## Field work, collection and transport

Field conditions	Fossils were discovered eroding from an exposure on the eastern side of Lake Turkana
Location	Area 103, Koobi Fora, Kenya
Access & import/export	Exploration and NACOSTI permits to Louise Leakey and Koobi Fora Research Project
Disturbance	Excavation of eroding outcrop

## Reporting for specific materials, systems and methods

We require information from authors about some types of materials, experimental systems and methods used in many studies. Here, indicate whether each material, system or method listed is relevant to your study. If you are not sure if a list item applies to your research, read the appropriate section before selecting a response.

### Materials & experimental systems

- n/a  Involved in the study
- Antibodies
  - Eukaryotic cell lines
  - Palaeontology and archaeology
  - Animals and other organisms
  - Clinical data
  - Dual use research of concern
  - Plants

### Methods

- n/a  Involved in the study
- ChIP-seq
  - Flow cytometry
  - MRI-based neuroimaging

## Palaeontology and Archaeology

- Specimen provenance
- Specimen deposition
- Dating methods
- Tick this box to confirm that the raw and calibrated dates are available in the paper or in Supplementary Information.
- Ethics oversight

Note that full information on the approval of the study protocol must also be provided in the manuscript.

## Plants

- Seed stocks
- Novel plant genotypes
- Authentication